Chapter 3

Effect of rheological models on pulsatile hemodynamics in a multiply afflicted descending human aortic network

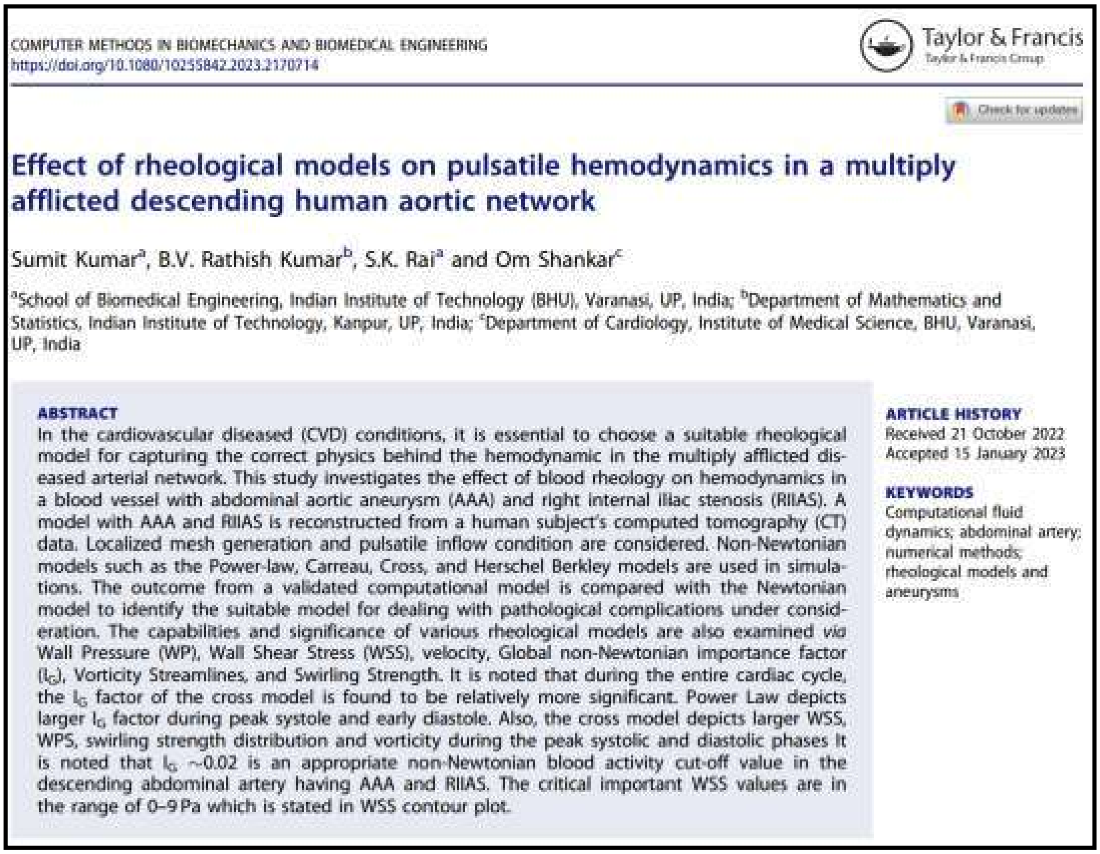

COMPUTER METHODS IN BIOMECHANICS AND BIOMEDICAL ENGINEERING
https://doi.org/10.1080/10255842.2023.2170714

Effect of rheological models on pulsatile hemodynamics in a multiply afflicted descending human aortic network

Sumit Kumar[a], B.V. Rathish Kumar[b], S.K. Rai[a] and Om Shankar[c]

[a]School of Biomedical Engineering, Indian Institute of Technology (BHU), Varanasi, UP, India; [b]Department of Mathematics and Statistics, Indian Institute of Technology, Kanpur, UP, India; [c]Department of Cardiology, Institute of Medical Science, BHU, Varanasi, UP, India

ABSTRACT

In the cardiovascular diseased (CVD) conditions, it is essential to choose a suitable rheological model for capturing the correct physics behind the hemodynamic in the multiply afflicted diseased arterial network. This study investigates the effect of blood rheology on hemodynamics in a blood vessel with abdominal aortic aneurysm (AAA) and right internal iliac stenosis (RIIAS). A model with AAA and RIIAS is reconstructed from a human subject's computed tomography (CT) data. Localized mesh generation and pulsatile inflow condition are considered. Non-Newtonian models such as the Power-law, Carreau, Cross, and Herschel Berkley models are used in simulations. The outcome from a validated computational model is compared with the Newtonian model to identify the suitable model for dealing with pathological complications under consideration. The capabilities and significance of various rheological models are also examined *via* Wall Pressure (WP), Wall Shear Stress (WSS), velocity, Global non-Newtonian importance factor (I_G), Vorticity Streamlines, and Swirling Strength. It is noted that during the entire cardiac cycle, the I_G factor of the cross model is found to be relatively more significant. Power Law depicts larger I_G factor during peak systole and early diastole. Also, the cross model depicts larger WSS, WPS, swirling strength distribution and vorticity during the peak systolic and diastolic phases It is noted that I_G ~0.02 is an appropriate non-Newtonian blood activity cut-off value in the descending abdominal artery having AAA and RIIAS. The critical important WSS values are in the range of 0–9 Pa which is stated in WSS contour plot.

ARTICLE HISTORY
Received 21 October 2022
Accepted 15 January 2023

KEYWORDS
Computational fluid dynamics; abdominal artery; numerical methods; rheological models and aneurysms

Chapter 3

Effect of rheological models on pulsatile hemodynamics in a multiply afflicted descending human aortic network

3.1 Introduction

In the human body, the abdominal aorta is the largest artery. It receives cardiac output from the left ventricle and delivers oxygenated blood to the body via systemic circulation. Ascending aorta, aortic arch, thoracic (descending) aorta, and abdominal aorta are the four divisions of the aorta. The descending abdominal aorta has an intricate geometry, including non-planar curvature, branches at lumbar, renal, iliac and significant tapering with distensible vessel walls. Many studies on cardiovascular system modelling and simulation have been conducted utilizing medical imaging data and CFD (Hazer et al., 2006; Kim et al., 2008; Taylor and Figueroa, 2009) (Carvalho et al., 2021; Faraji et al., 2022; Ferdows et al., 2022; Javadzadegan et al., 2017). CFD is a numerical method that solves tightly coupled non-linear conservation equation like continuity and Navier-Stokes equations, to obtain physical properties of mass and momentum, such as velocity and pressure of fluid flow. CFD was first used in the medical field in the 1990s. With the emergence of diagnostic imaging technologies such as computed tomography (CT), MRI, and digital subtraction angiography (DSA) in the 2000s, patient-specific simulations emerged. Recently many work reported using CFD for analysis of blood flow in cardiovascular system. (Caballero and Laín, 2015; Kadhim et al., 2018; Kamada et al., 2022; Khalafvand et al., 2011; Kharboutly et al., 2005; Linge et al., 2014; Moosavi et al., 2014; Rispoli et al., 2015; Wu et al., 2015;

Zhong et al., 2018). The viscosity of blood can affect the hemodynamic features of blood flow in an arterial network. Various researchers pointed that plasma acts as a Newtonian fluid (Schobeiri, 2010), while the whole blood has a non-Newtonian character (Thomas and Sumam, 2016b). In routine human circulation, blood flow inside the artery, if unusual hemodynamic conditions arise, can generate an abnormal biological response. Blood viscosity is an essential parameter for the investigation of flow dynamics. The viscosity of blood depends on the plasma and hematocrit (Ht) viscosity (Siauw et al., 2000). Since it is well-known fact that if the shear rate is larger than 100 $S^{-1,}$ then blood acts as a Newtonian fluid having constant viscosity. However, if the shear rate of the blood flow drops below this threshold, its viscosity increases, and non-Newtonian fluid behavior starts to show up. Many research work has been done regarding shear thinning characteristics effect of blood (Anand and Rajagopal, 2004; Cherry and Eaton, 2013; Fatahian et al., 2018; Nader et al., 2019; Sochi, 2013). The study by (Kumar and Deoghare, 2018) depicted the importance of Newtonian models in blood flow simulations by adopting a reconstructed model from CT scan. The non-Newtonian effects in patient-specific models were analyzed by some authors in abdominal artery (Abbasian et al., 2020a; Ahsaas and Tiwari, 2016; Karimi et al., 2014b), carotid arteries (Chen and Lu, 2004a; Nagargoje et al., 2021; Seo, 2013) and coronary arteries (Pandey et al., 2020b, 2020a; Ryou et al., 2012; Vinoth et al., 2016).The experimental studies by E. Boutsianis et al. and N.D. Nguyen et al. (Boutsianis et al., 2009b; Nguyen and Haque, 1990) prove that blood flow should be a non-Newtonian viscous model. It has been found that the circulation of reversed flow and WSS are the key factors in the growth of stenosis and aneurysms (Alishahi et al., 2011),(Gay and Zhang, 2009). However, the predicted hemodynamics characteristics of the various Newtonian and non-Newtonian blood flow models are still debatable. In Figure 3.1 (a) & (b) , the apparent viscosity versus strain rate of five significant rheological models are related with the experimental data of Merrill (Errill, 1969), Biro (Biro, 1982) and Skalak et al. It is to be noted that the trend line for the cross model follows a track analogous to the other experimental and rheological models with some deviations across the lesser and higher ranges of shear rate. The Carreau model is consistent with the experimental data of Biro (Biro, 1982), particularly for the shear rates $\dot{\gamma} < 10\ S^{-1}$. It also depicts that because of transient flow and complex geometry, the viscosity behavior also changes. In cardiovascular system, naturally blood flows in a pulsatile nature in cardiac cycle consisting systolic and diastolic phase. For patient-specific models study it is important to consider real physiologically relevant boundary condition like pulsatile inflow to trace the correct hemodynamics conditions for various non-Newtonian models significant for blood flow analysis which has been considered many prior work (Johnston et al., 2006, 2006; Karimi et al., 2014a; Les et al., 2010)(Kumar et al., 2022) (Boyd et al., 2007; Hammoud et al., 2019; Jahangiri et al., 2015; Perktold et al., 1991). Investigation of Sutter by nanofluid , biomedical simulations of rheological models and nanoparticle in blood flow are studied by (Abdelsalam et al., 2022; Abdelsalam and Zaher, 2022; Alsharif et al., 2022; Faizan et al., 2022; Mekheimer et al., 2022; Sridhar et al., 2022).

Hence in this study, which is aimed at unraveling the physics behind the pulsatile flow in a multiply afflicted arterial network with significant morphological deviations from regular geometry, the five important rheological models are numerically simulated to investigate the hemodynamic parameters to decide on a suitable model for patient specific data blood flow analysis. In the case of an artery with both aneurysm and stenosis, selection of right blood rheological model plays an important role in correctly tracing the hemodynamic features in the artery under several pathological conditions.

It is found from the previous studies that substantial volume of work on patient-specific and idealized geometry-based blood flow numerical simulation in healthy and diseased arteries but there has been little reporting on numerical analysis of flow in vessels associated with numerous cardiovascular illnesses such as abdominal aortic aneurysm (AAA) and right internal iliac artery stenosis (RIIAS). AAA and lower extremity disease (LEAD), such as RIIAS, are two of the most serious arterial illnesses affecting the cardiovascular system (Wong et al., 2012),(Mahé et al., 2015), and they need to be addressed thoroughly in 3D with realistic clinical data. Also, it has been found that in descending abdominal aorta, the analysis of non-Newtonian blood rheology has not been explored for its potential in defining the hemodynamic parameters across the variable arterial length and diameter. Therefore, an effort has been made to examine the behavior of various rheological models in a realistic 3D model of an artery with both AAA and RIIAS based on CT subject data in order to enrich, sharpen, and improve the clinical diagnostic information pertinent to the complicated arterial disease.

The study shows a comprehensive representation of the transient flow dynamics of five important rheological models at different cardiac time steps using physiological/clinically recorded pulsatile input data. A healthy abdominal artery is initially created using patient-specific CT scan data. A new model of an artery is created by using the available design data for aneurysms and stenosis. This model has one inlet and nine distinct outlets, including AAA and RIIAS. For boundary conditions, pulsatile velocity inlet profiles were incorporated, and the effect of five viscosity models of blood flow has also been studied. The effects of several rheological models are evaluated using WSS, vorticity, swirling strength, central line velocity (CLV), velocity contour, streamlines, central line pressure (CLP), and wall pressure (WP), as detailed in the results. The numerical simulations are offered to aid cardiologists as diagnostic tools in the field of medicine. This will aid in the early diagnosis and treatment of aneurysms (e.g., AAA) complicated by stenosis (e.g., RIIASS) in arterial networks with several branches.

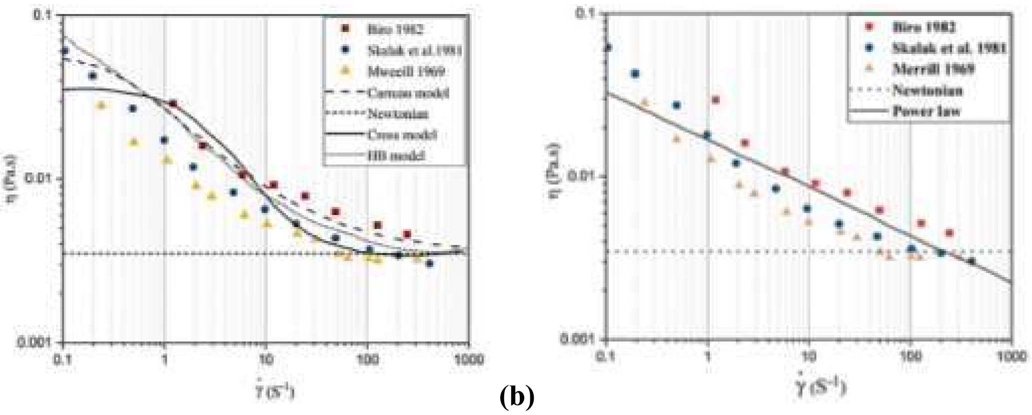

(a) **(b)**

Figure 3.1: Apparent blood viscosity versus shear rate for different rheological models and experimental data by Merrill, Biro, and Skalak et al. (a) Carreau, Cross and HB model (b) Power-law type.

3.2 Methods

3.2.1 Geometric model

A three-dimensional patient-specific model is created using a CT image of the abdomen of an 80-year-old male (128 slices, GE medical system, CT scan centre, IMS

BHU, Varanasi, India). With 512×512 image matrices, 0.9609 mm pixel size, and 1.25 mm thickness, the aorta to the lower belly region was scanned. The "Materialize MIMICS V18" medical image modelling programme is used to generate a 3D model using patient-specific two-dimensional slice data. First, a healthy 3D model of the artery is created as a reference, then it's turned into a AAA & RIIAS-infected one. The aneurysm (AAA of 47%) and stenosis (RIIAS of 91%) are combined in the same vascular geometry, setting D/La to 0.47 and D/Ls to 0.91 (Kumar et al. 2022). To examine the blood flow dynamics in the developed 3D complicated vascular network model, different cross-sections are selected shown in (Figure 3.2). These cross-sections (S1 to S12) are away from the inlet and outlet to avoid boundary conditions. The space claim module converts STL basic geometry into solid form for computational blood flow simulations. It needs to be emphasized that the biologically established Reynolds number for the arterial network under examination is in the range of 1400-1600 at peak systolic phase and 300-500 during diastolic phase. The details on the processing (solver setup, BC setup) and post-processing steps Non-Newtonian Indicating Factor (NNIF), result extraction and analysis, validation etc., are also provided in further sections.

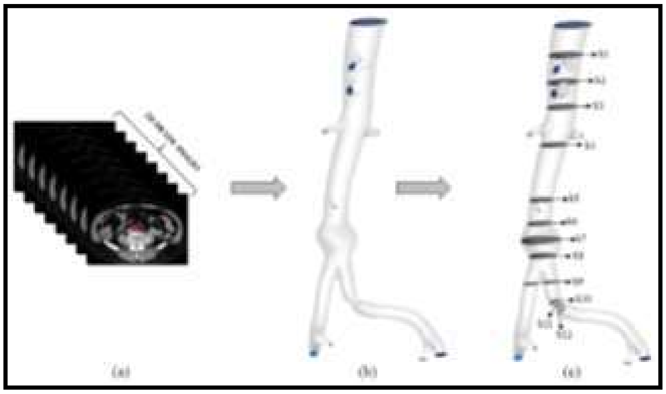

Figure 3.2 : Reconstruction of the three-dimensional model using CT-scan DICOM image (a) segmentation of region of interest (b) 3D model of artery (c) Various sectional place considered in AAA and RIIAS region.

3.2.2 Governing equations for blood flow simulation

The equations regulating mass and momentum conservation in Newtonian and non-Newtonian incompressible fluid flow are described by:

$$\nabla . U = 0 \tag{1}$$

$$\rho \left(\frac{\partial u}{\partial t} + \nabla . (uU) \right) = - \frac{\partial p}{\partial x} + \frac{\partial (\tau_{xx})}{\partial x} + \frac{\partial (\tau_{yx})}{\partial y} + \frac{\partial (\tau_{zx})}{\partial z} + \rho f_x \tag{2}$$

$$\rho \left(\frac{\partial v}{\partial t} + \nabla . (vU) \right) = - \frac{\partial p}{\partial y} + \frac{\partial (\tau_{xy})}{\partial x} + \frac{\partial (\tau_{yy})}{\partial y} + \frac{\partial (\tau_{zy})}{\partial z} + \rho f_y \tag{3}$$

$$\rho \left(\frac{\partial w}{\partial t} + \nabla . (wU) \right) = - \frac{\partial p}{\partial z} + \frac{\partial (\tau_{xz})}{\partial x} + \frac{\partial (\tau_{yz})}{\partial y} + \frac{\partial (\tau_{zz})}{\partial z} + \rho f_z \tag{4}$$

$$\tau = \mu (\nabla U + (\nabla U)^T) \tag{5}$$

Where U is the velocity vector given by *U* = (u,v,w) with u,v,w denoting the three velocity components, t is time, ρ is the fluid density, p is hydrostatic pressure, τ is shear stress and dynamic coefficient of viscosity is given by

$$\mu = \mu(\dot{\gamma}) \tag{6}$$

Where $\dot{\gamma}$ is the shear rate. For different rheological models, t μ the dynamic coefficient of viscosity is defined differently based on their constitutive laws, as shown in Table 3.1.

Table 3.1 Effective viscosity equations of various rheological models with their parameters.

S.no	Rheological model	Effective viscosity equations	Parameters
01	Newtonian	$\mu = \mu_\infty$	$\mu_\infty = 0.0035\ Pa.s$
02	Carreau (Cho and Kensey, 1991)	$\mu = \mu_\infty + (\mu_0 - \mu_\infty)[1 + (\lambda\dot{\gamma})^2]^{\frac{n-1}{2}}$	$\mu_0 = 0.056\ Pa.s\ , \lambda = 3.313s$
03	Power (Hsu et al., 2009)	$\mu = \eta(\ddot{\gamma}) = k\ (\dot{\gamma})^{n-1}$	k= 0.017, n= 0.708
04	Herschel Bulkley (Antonova, 2012)	$\mu = \frac{\tau_0}{\lvert\gamma\rvert} + k\lvert\dot{\gamma}\rvert^{n-1}$	$\tau = 0.091\ Pa$ K $= 0.0146$ Pa.s , n $= 0.81$
05	Cross (Hsu et al., 2009)	$\mu = \mu_\infty + \frac{\mu_0 - \mu_\infty}{[1 + (\lambda\dot{\gamma})^n]^a}$	$\mu_0 = 0.0364\ Pa.s, \lambda = 0.38\ s$ $\mu_\infty = 0.00345\ Pa.s, n = 1.45$

3.2.3 Non-Newtonian rheological models for blood

Few of the popular rheological models of blood, primarily characterizing the stress-shear rate relation, are depicted by the appropriate definition of μ in Table 3.1. Here, we consider the Newtonian and four most reputable non-Newtonian models viz., Carreau, Power Law, Herschel Berkley, and Cross for modelling the stress-shear rate relation of blood. The corresponding constitutive laws with their parameters are also mentioned in Table 3.2.

In the Newtonian model, μ is treated to be a constant. In Carreau models, λ represents the relaxation time constant with a unit of second (s). At higher shear rates (above 100 s^{-1}), The viscosity of the Carreau model is close to that of the Newtonian model, and it also fits well with the results of experiments (Cho and Kensey, 1991). The Cross model is the simplified form of the Carreau model (Karimi et al., 2014b) . The comparison of experimental and computational apparent viscosity versus strain rate is shown in (Figure 3.1 (a) & (b)) . The Cross model, also known as the Bird-Carreau model, is the simplified form of the Carreau model, which can be a good candidate for modelling the blood flow in large arteries due to the shorter range of viscosities generated by the model.

Similarly, the power model is appropriate for the middle range of shear rates. It does not define the blood behavior separately in the low and high shear rate regions into the intima, which accelerates atherosclerosis plaque formation. The non-Newtonian model is known to have an impact on intra-cardiac blood flow. The blood rheology as described by the Herschel-Bulkley model (Jahangiri et al., 2015) has also been considered, for understanding its relative stance in describing the hemodynamics under the current computational explorations on the relevance of various rheological models in a complex arterial network.

3.2.4 Initial and boundary conditions

At the inlet a clinically determined inflow condition has been prescribed. The physiologically true transient and pulsatile inlet velocity profile that has been selected from literature (Vasava et al., 2012)'(Jozwik and Obidowski, 2010)'(Kim et al., 2004). The stress-free outflow boundary condition is applied at all the outlets of the descending abdominal artery as depicted by Karimi et al. (Karimi et al., 2014a). The no-slip boundary conditions on the non-compliant walls are implemented in the solver.

3.2.5 Discretization and mesh independency check

The innovative local mesh methodology is used to mesh the geometry. Local meshing begins with the establishment of local coordinates for the purpose of identifying corresponding spheres of influence in regions that must be meshed locally. Later, all of the selected local zones inside the spheres of influence are meshed using a sizing technique. According to the literature on image-based complicated shapes, a tetrahedral element is the best fit (Boutsianis et al., 2009b, 2009c). Hence, the tetrahedral element is used in this model. To achieve more accurate results near the artery wall, five inflation layers with a growth rate of 1.2 are established.

For the grid independence test, three generations of mesh elements are selected: coarse (3 mm), moderate (2 mm), and fine (1 mm). The grid independence test mesh parameters are listed in Table 3.2. Maximum velocity at nine outlets in each of the three mesh models is compared for the grid independence test, and the results are confirmed. Since switching from an intermediate grid to a fine mesh results in a less than 1% variation in maximum velocities at all nine outputs, all numerical simulations are carried out on fine mesh with 1358804 nodes and 5513363 elements.

Table 3.2. Mesh details of geometry

Mesh sizes	Number of Elements	Number of nodes
Mesh1 (1mm size)	5513363	1358804
Mesh2 (2 mm size)	3054057	796934
Mesh3 (3 mm size)	2740574	712229

3.2.6 Simulation setup

For the simulation setup, blood flow is supposed to be laminar, single-phased, and transient. The CFD numerical simulations are based on the finite volume method (FVM). As suggested and illustrated by (Karimi et al., 2014b) the stress-free outflow boundary condition is implemented at all the outlets of the descending abdominal artery network with bifurcations. All the above mentioned five different rheological models for blood flow have been assessed for their relevance in unravelling the hemodynamics under compounded pathological conditions in a realistic, complex arterial network. The ANSYS-FLUENT solver is used to solve the above governing equations of blood flow through multiply afflicted descending human aortic network Using the SIMPLE algorithm and a second-order upwind technique for convective terms and a cell-centered approximation for pressure gradients, the velocity-pressure coupling is spatially discretized. The SIMPLE algorithm uses a link between velocity and pressure corrections to make sure that the mass stays the same and get the pressure field. The new Fluent FVM modules-based CFD simulations are done on a workstation with 48 cores, 64 GB of RAM, and an 8 GB graphics card. Near the vessel wall, the velocity field is precisely controlled by a thin grid with a thickness of 0.1 mm and a rate of growth of 1.2. A localized meshing method with 0.25 mm elements is used at different local coordinates. The transient flow analysis is done with a 0.01-ms time step and the first-order implicit Euler method. The convergence bounds for residuals are set to 10^{-4} for all equations, and each time step produced well-converged results. All simulations in this study are conducted for at least three cardiac cycles, or until the solution reaches a periodic condition. In the following section, flow simulation results for one complete cycle are provided and discussed.

3.2.7 Validation

In the present study to validate our computational model we designed idealized geometry based on previous experimental work on abdominal aneurysms by Patel et al (Patel et al., 2017). The inlet diameter d_i and outlet diameter d_o of the model, both have an inner diameter of 16 mm. The maximal inner diameter and length of the aneurysm, respectively, are D and L. The aneurysm is axisymmetric, with a dilation ratio of $D/d_i = 2.5$ and an elongation ratio of $L/d_i = 4$. The dimension used here are of typical fusiform aneurysms (Egelhoff et al., 1999). Also, the length of straight tube is 90mm i.e. adequate enough for the flow to become fully established before entering aneurysms. By resolving the mass and momentum balance equations for the fluid phase, steady flow Peak Reynold number (R_e=1350) in a symmetric tubular bulge has been designed and simulated. Experimental results are validated against numerical predictions by comparing the in-plane flow pattern produced here with the one experimentally obtained by Patel et al (Patel et al., 2017).The simulation's fluid characteristics (density = 1156 kg/m3, kinematic viscosity = 7.39 106 m2/s1) match those of the tests. At the inflow boundary, the velocity circulation is uniform and pressure is extrapolated from the interior; meanwhile, at the outflow boundary, a constant pressure (P = 0) is imposed and velocities are extrapolated from the interior by a zero-gradient condition. Tetrahedral cells are used to discretize the computational domain and grid independency validation also performed by using four different mesh sizes of 0.5 mm, 1mm, 2 mm and 3 mm as depicted in Figure 3.3 (a-c). The incompressible Navier-Stokes equations are used to simulate a three-dimensional flow field based on a finite-volume code. Three parts of the bulge's axial velocity profiles, shown in Figure 3.3 (g-i) exhibit a good match between experimental data and computational estimates by Patel et al (Patel et al., 2017).

Also, the two approaches' results are in good accord, and they show that the flow is characterized by a central core flow surrounded by sizable recirculation zones on both sides as depicted in (Figure 3.3 (f)).

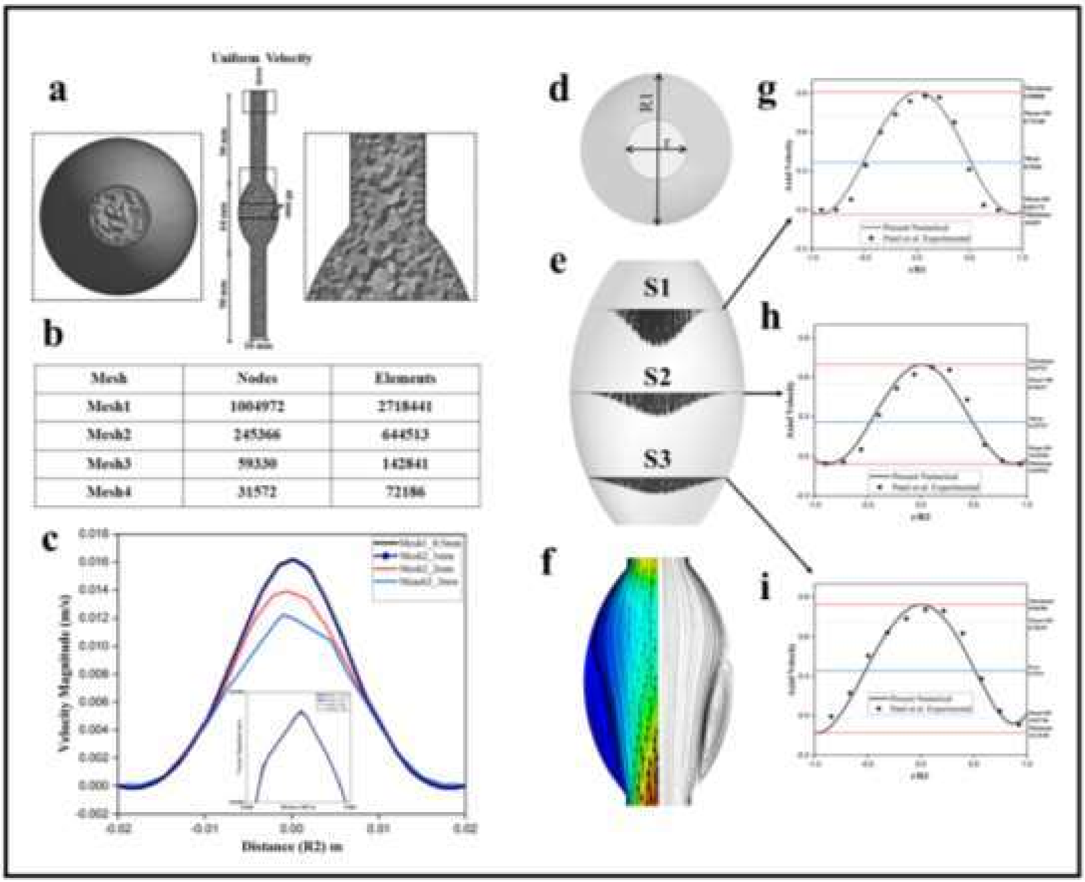

Mesh	Nodes	Elements
Mesh1	1004972	2718441
Mesh2	245366	644513
Mesh3	59330	142841
Mesh4	31572	72186

Figure 3.3 : (a) Symmetricity mesh description of the AAA geometry for numerical simulation. (b) Mesh table of four mesh size Mesh1 (0.5mm), Mesh2 (1mm), Mesh3 (2mm) and Mesh3 (3 mm) (c) Mesh validation (d) Symmetric circle visualization (e) Velocity vectors on three axial plane S1, S2 and S3 (f) Velocity streamlines (g-i) Sections 1–3 (for y* = = y L 0.2, 0.5 and 0.8 respectively) at which non-dimensional axial velocity profiles are compared and velocity vectors of respective sections is plotted under steady flow conditions also comparison of numerical and experimental axial velocity profiles at the selected sections with Patel et al.

3.3 Results

In this study blood flow dynamics due to different rheological models in terms of Velocity contours, Wall Shear Stress (WSS), Wall Pressure (WP), Swirling strength, Core Vorticity and Non-Newtonian effect factors have been studied to compare the effects of aneurysms and stenosis in the same arterial network. There are two phases to the cardiac flow cycle. The first phase, when the flow speeds up, is called the systolic phase. The second phase, when the flow slows down after the systolic phase, is called the diastolic phase. Results at the next six important times are tracked to figure out how transient blood flow works.:

- T_1 = 0.1 s at the start of the systole and late of diastole instant
- T_2 =0.2 s at the mid accelerating phase of systole
- T_3 =0.3 s at peak systole
- T_4 =0.4 s at the middle of the decelerating systolic phase with the same velocity as T_2
- T_5 =0.5 s at the end of the decelerating phase of systole
- T_6 =0.6 s at the start of the diastole instant

3.3.1 Centerline velocity and pressure profile during the peak of systole

3.3.1.1 Centerline velocity

The peak systolic axial velocities along the centerline corresponding to all the five rheological models for $-0.23\ m \leq Z \leq -0.33\ m$, especially covering the AAA and RIIAS regions, are shown in (Figure 3.4). At the peak systole, the velocities corresponding to the Newtonian model are relatively higher in magnitude than that of the other four models. The peak systolic velocities corresponding to the cross and carreau models are closer to each other. The velocity magnitudes corresponding to the power law model are seen to be the least and is immediately followed up by those corresponding to the Herschel model. While the velocities in the AAA region, from the different models, are lower and vary between 0.05 m/s to 0.2 m/s. They are noted to be significantly higher in RIIAS region with a variation between 0.3 m/s to 0.9 m/s. Such a variation is due to the morphological variation in the vessel dimension due to AAA and RIIAS. These geometrical variations, which is relatively more w.r.t. RIIAS, brings in a break in the gradient flow leading to a fall or raise in velocities. Further, post stenosis, there is a sudden fall in velocity magnitude because of spatial variation and sharp peaks in velocities due to tapering and curvature effects. It is noticed that in the double afflicted diseased model, there is significant variation in velocity curve response in all five models during the peak of systole; however, the cross model is closer to the Newtonian model in terms of trendline and behavior.

3.3.1.2 Centerline pressure

(Figure 3.5) depicts the centerline pressure distribution due to the five rheological models at the peak of the systole. By investigating the response of centerline pressure (CLPs) for all the five viscosity models during the cardiac cycle, it is found that CLPs significantly vary across the entire cycle, but at the peak of systole, it shows larger variations. It is noted that the Power Law Model pressures are significantly greater than those from other rheological models. While the pressures of Hershcel and Carreau Models are closer and fall below those of the Power Law Model, the pressures associated with the Cross and Newtonian Models are closer and are relatively smaller than those from other models. Also, it is to be noted that in the region on AAA, the pressure magnitude is higher; however, in the region of RIIAS, there is an adverse gradient in pressure due to the stenosed condition. Also, post stenosis, there is a raise in pressures coming from all the five rheological models which is very much in tune with the central line velocity fall noticed in (Figure 3.3.1.1). To ensure such a rapid variation in flow dynamics during peak systole, simulations are repeated for several cardiac cycles to accurately trace the physics behind the pulsatile flow.

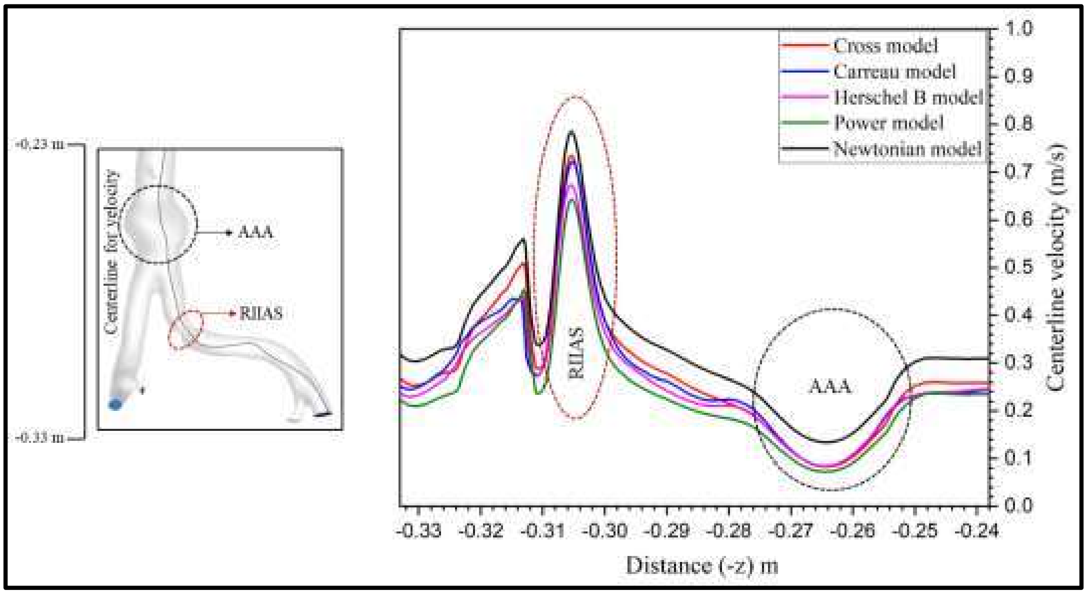

Figure 3.4 : Velocity distribution of five rheological models along centerline line from plane S5 at z = -0.23 m to -0.33 m during peak of systolic phase i.e., at T_3 = 0.3 s.

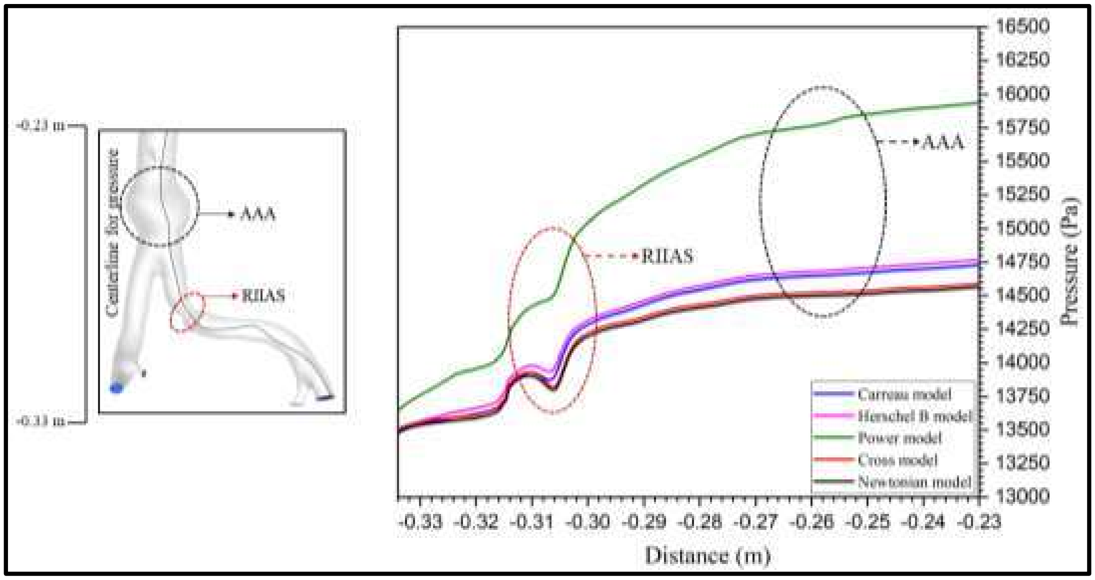

Figure 3.5 : Centerline pressure distribution of five rheological models from plane S5 at z = -0.23 m to -0.33 m during the peak of systolic phase, i.e., at T_3 = 0.3 s.

3.3.2 Wall shear stress effect during crucial cardiac instant

(Figure 3.6 (a-c)) illustrate variations of WSS for five rheological models at three significant instants of the cardiac cycle, i.e., at peak systole (T_3), mid of systolic deceleration (T_5) and end of systole (T_6). WSS magnitudes are plotted along the curve AB on the surface of the wall starting from section S5 at Z = - 0.20 m to the end of the right iliac bifurcation. An oscillation in the WSS during the entire cardiac cycle is noticed in all models. At the peak of systole as shown in Figure 3.6 (a) the WSSs corresponding to the Cross and Power models are higher than the other three rheological models all along the curve AB. In the AAA region, due to the vessel wall dilation, a fall in localized WSS magnitudes (i.e. from 20 to 5 Pa) sensitive to the blood rheological model is noticed. Such a dip in WSSs are found to be dominant with Cross and Power models. Beyond the AAA region, many oscillations with dominant peaks in RIIAS region are observed in the WSSs, due to the blood vessel geometrical change induced flow variations in all models. The localized rheology-based variations especially in the RIIAS region such as spatial lag in the peak WSS manifestation, oscillatory peaks and downstream post-stenotic region oscillatory WSSs can be attributed to the flow complexities such as separation, vortex formation, vessel curvature flow swirling etc. The post stenotic region WSSs of Cross and Power models are both markedly oscillatory and considerably large.

During mid-systolic deceleration, i.e., at T_5 from Figure 3.6 (b) one can notice significant variations in WSSs primarily in the AAA and the RIIAS regions. In the AAA region a fall in WSSs, from around 8 Pa to around 0 Pa, corresponding to all the rheological models is noticed with relatively larger WSSs at the head and toe of the aneurysm. A significant raise in WSSs, in the range of about 10 Pa to 65 Pa, is noticed in the RIIAS region with different models. A dominant raise in WSSs corresponding to the Cross, Power and Newtonian models is noticed in that order. Also, the spatial location of the peak WSS in RIIAS region is found to be sensitive to the blood rheology. While the spatial location of peak WSSs corresponding to Cross Model lies on upstream part of the RIIAS region the same for the Power and Newtonian models are located around the mid-section and the downstream side of the RIIAS region respectively. Also, significant secondary fluctuations in WSSs corresponding to Cross, Power and Newtonian models are noted adjacent to the primary dominant peaks within the RIIAS region. Further downstream to the RIIAS region WSSs, especially corresponding to these three models, are oscillatory with sharp peaks, though relatively smaller than those noticed in the RIIAS region. Clearly these complex variations in WSSs indicate potential flow complexities in these regions and a demand a detailed probe on the pulsatile flow dynamics for substantiating the same.

Figure 3.6 (c) depicts the spatial variation in WSS towards the end of the systole (T_6). Clearly, irrespective of the blood rheological model, the WSSs continue to remain considerably large in the RIIAS region. The WSSs corresponding to the Cross, Power and Newtonian models, though slightly smaller in magnitude than those seen during T_3 and T_5, continue to stay larger over those from other models in that order. Also, the spatial location of these large WSS bands vary with the rheology model for the blood within the RIIAS region. While the WSS in the RIIAS region shoot from 6Pa to 45 Pa those in the AAA region go down from 6 Pa to 0 Pa. Also, at this time of the systolic phase, the AAA region WSSs of all the models get quite close.

Further during the late systolic phase secondary oscillations are seen to manifest in the RIIAS region downstream to the large primary WSS bands. Downstream to the RIIAS region, WSS continue to remain significant possibly owing the flow complexities.

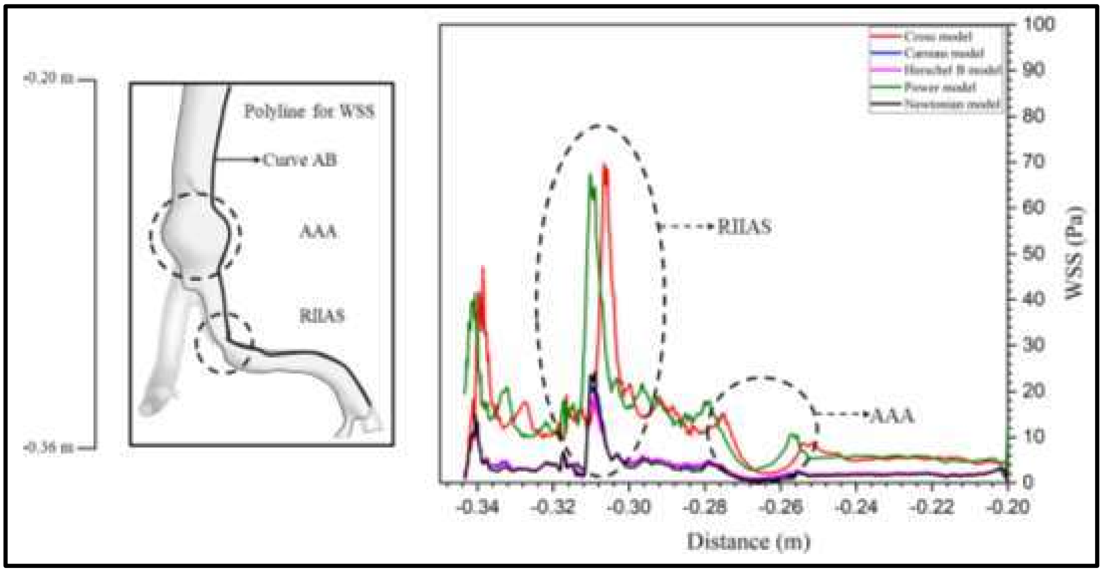

(a)

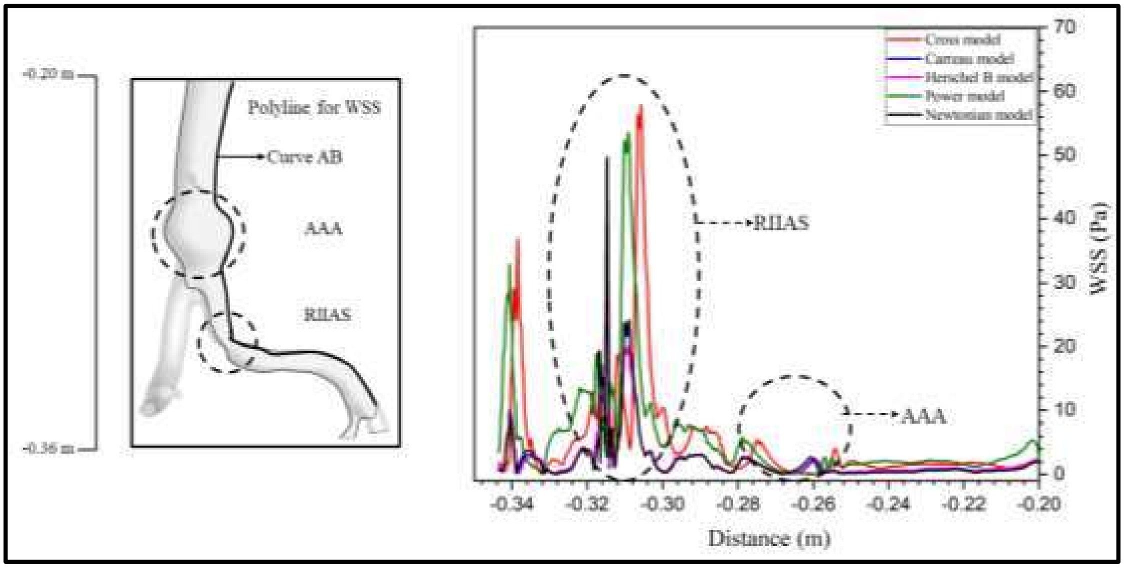

(b)

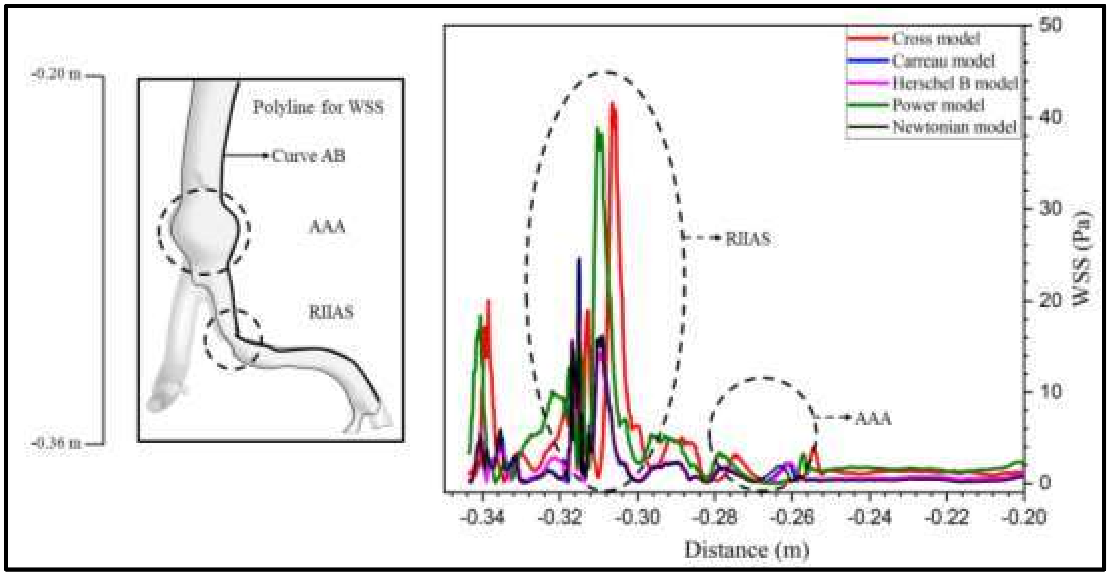

(c)

Figure 3.6 : Wall shear stress distribution of five rheological models along medial plane wall i.e., on right side of artery from section S5 to the outlet of the artery to the end of outlet Z = -0.36 m during (a) peak of systolic phase T_3= 0.3 s (b) mid of deceleration phase of systole T_5= 0.5 s (c) end of systole T_6= 0.6 s.

3.3.3 Wall pressure (WPs) effect during crucial cardiac instant

Plots in Figure 3.7 (a, b, and c) depict the distribution of wall pressure (WPs) along the same line as in the WSSs scenario shown in Figure 3.6 (a), (b) & (c). During the peak of systole in Figure 3.7 (a) a substantial pressure gradient arises from -0.20 m to -0.33 m w.r.t all the models though they are considerably (about 1.5 times) large for the Cross and Power viscosity models. While the pressure drop is largest for the Cross Model the smallest pressure drop is noticed with the Newtonian model. Also, while the pressure drop of the Power model is close to that of the Cross model the pressure drops w.r.t other two models are close to the Newtonian case, though larger than that of Newtonian case.

During the mid-systolic phase i.e. at T_5 the WPs, w.r.t. all the models slowly raise from the inlet region till the RIIAS region. In this region, while the WPs corresponding to the Cross model and Power Law model are larger than those corresponding to the other models in that order. The WPs corresponding to the Newtonian model are found to be relatively small. In all the cases, the increase in the WPs especially in the AAA region, due to the wall dilation, very well agrees with the fall in the central line velocities in the same region noted earlier. In the RIIAS region oscillatory adverse pressure gradients are seen with all the models. While the Newtonian oscillatory adverse pressure gradients are the largest, the same of the Cross model, Power model, Herschel Buckley model and the Carreau model follow it in that order. Such an adverse pressure gradient variation calls for a thorough probe on the flow dynamics and this has carried out subsequently.

During T_6, in the upstream region starting from the inlet till the head of the RIIAS region there is an overall marginal dip in the WPs when compared to those during the T_5. However, in the AAA region one can continue to notice that the WPs raise up a bit as noted during mid-systolic deceleration. Now in the RIIAS region the oscillatory adverse pressure gradient continues to exist with again the values corresponding to the Newtonian model at lead followed by Carreau model, Herschel Buckley model, Power Law model and Cross model in that order. This variation in the pressure gradient oscillation differs from that noted during T_5 emphasizes the need for the right rheological model as the flow dynamics are sensitive to blood rheology. These complex

WP patterns indicates the presence of complex flow variation in this region and further downstream to the RIIAS.

In view of the above complex patterns in WSSs and WPs we now focus our attention firstly towards the surface WSSs and surface WPs and later move on trace the complex flow dynamics.

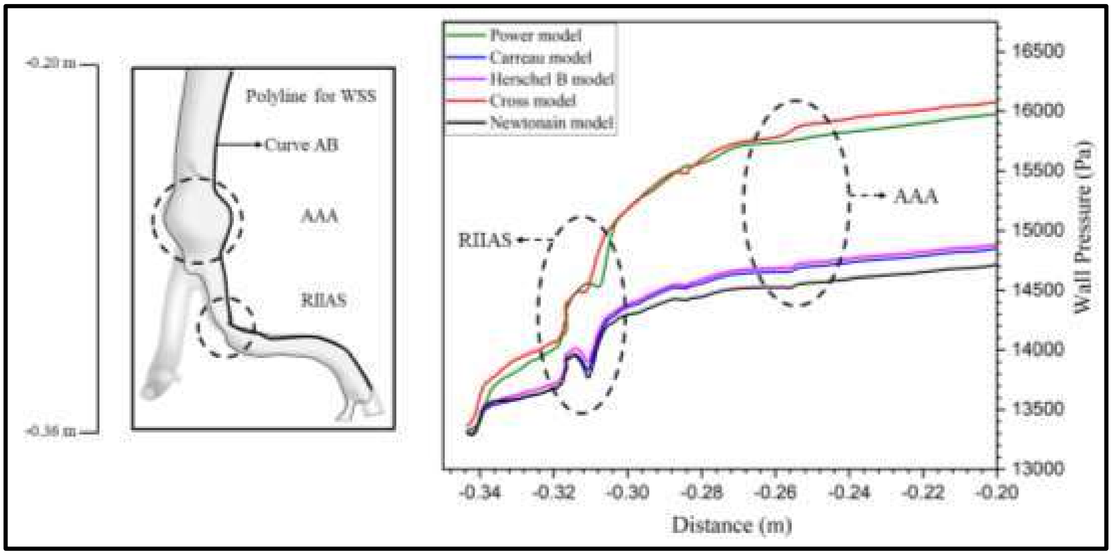

(a)

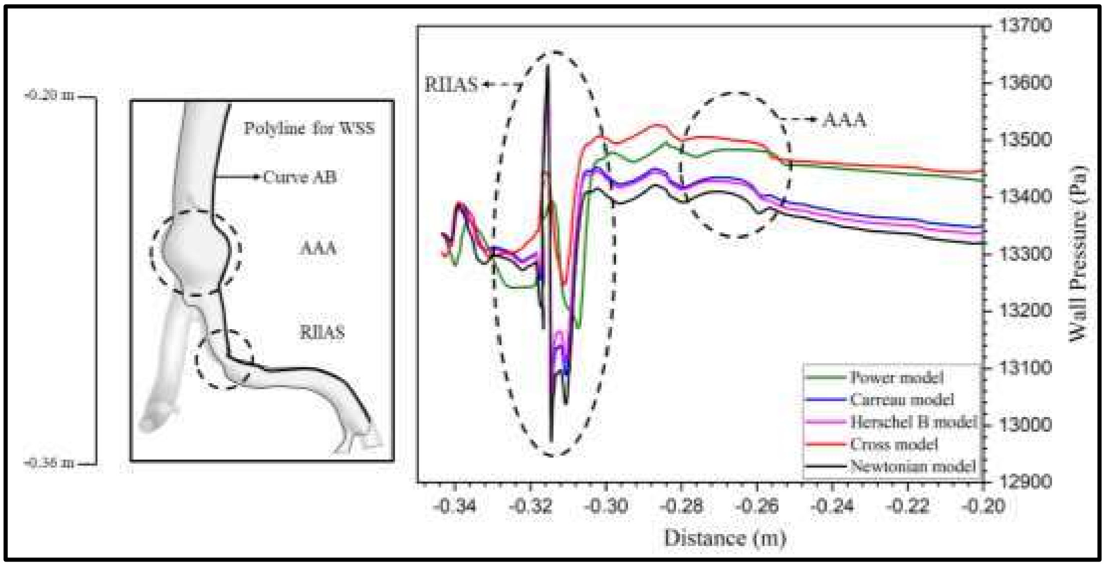

(b)

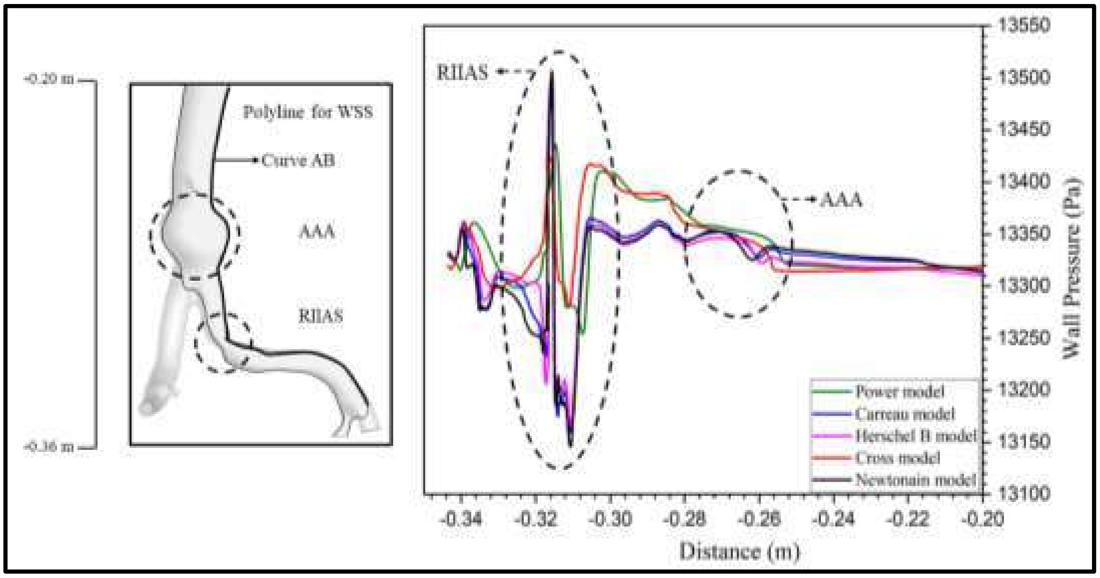

(c)

Figure 3.7 : Wall pressure distribution of five rheological models along medial wall contour i.e., on right side of artery from section S5 to the outlet of the artery to the end of outlet Z = -0.36 m during (a) peak of systolic phase T_3= 0.3 s (b) mid of deceleration phase of systole T_5= 0.5 s (c) end of systole T_6= 0.6 s.

3.3.4 Wall shear stress contour (WSS) distribution

Figure (3.8–3.12) depict the effect of five viscosity models on surface WSS distribution during pulsating cardiac flow cycle.

3.3.4.1 Cross model WSS

(Figure 3.8) illustrates the surface WSSs corresponding to the Cross model of the arterial network during the accelerating and decelerating phases of the cardiac cycle, i.e., from T_1 to T_6. From the onset to the end of the systole, it is observed that WSS attaints its peak at T_4 by gradually raising from T_1 through T_4 but significantly decrease after T_4, with the exception on the RIIAS region and near the outlet wall. The WSSs are relatively larger during systole on the head and toe regions of AAA, as well as across the wall of the RIIAS region and also in the region inferior to iliac bifurcations and those corresponding to the downstream to it near the outlets 3 and 4. During the decelerating phase, the WSSs are large near the wall of outlets 1, 2, 3, and in the RIIAS region. During T_1 through T_3, large WSS bands are noted in the head and toe regions of AAA with low WSSs in the hull region of AAA. In the case of RIIAS, WSSs are very large during the accelerating systole from the start of stenotic region to the peak stenotic section, but in the decelerating systolic phase they gradually decrease from T_4 to T_6. It is also noted that the large WSS bands, which appear to gradually diminish with systole, return during early diastole. Furthermore, it should be noted that scaled-WSS are more dominant in the right iliac stenosis zone than in the other regions of this sub-section. A large oscillatory scaled WSSs seen in both the AAA and RIIAS regions calls for special clinical attention.

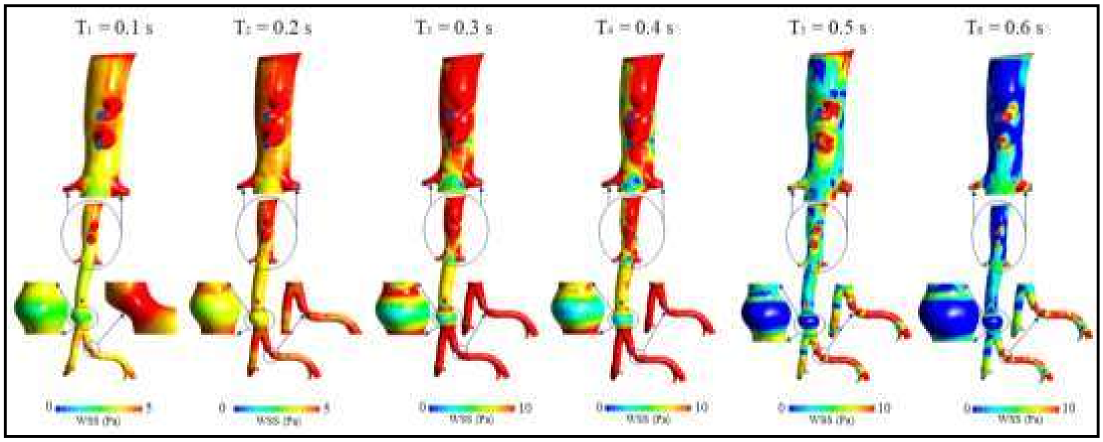

Figure 3.8 : WSS distribution along the aorta wall at the systole instants at T_1, T_2, T_3, T_4, T_5 and T_6 in the Cross model

3.3.4.2 Carreau model WSS

From the (Figure 3.9) corresponding to the WSSs of the Carreau model along the artery wall it is amply clear that during T_1 and T_2, the contours of WSS are nearly identical, with minor variations across the RIIAS region and very small WSSs in the AAA region. However, during T_3 and T_4, the intensity of WSS near the outlets 2, 3, 4, head and toe of AAA, RIIAS region and iliac bifurcation zone increase with spatial oscillations. The temporally oscillating maximum WSS are noticed in the localized pockets of AAA, RIIAS and iliac bifurcation regions during T_3 and T_4; and are of the order of 8.5 Pa.

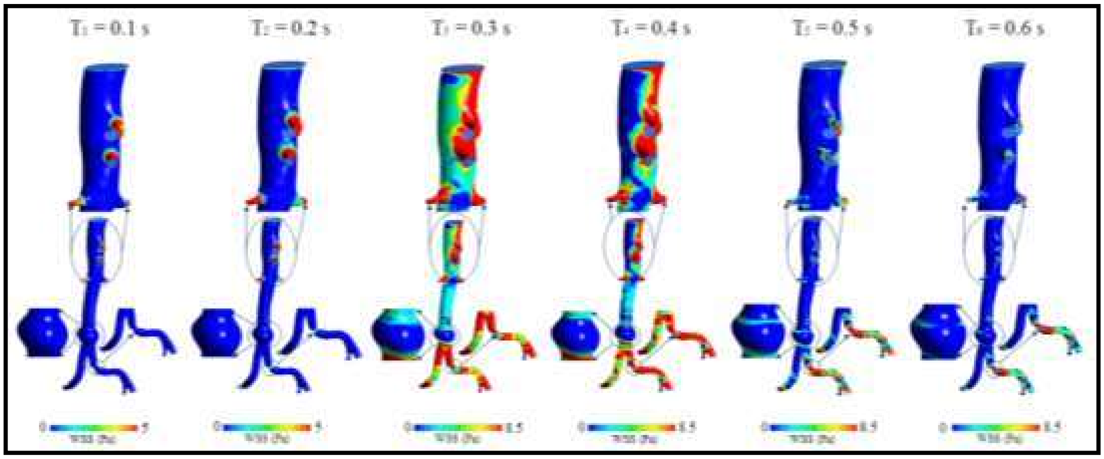

Figure 3.9 : WSS distribution along the aorta wall at the systole instants at T_1, T_2, T_3, T_4, T_5, and T_6 in the Carreau model

3.3.4.3 Power model WSS

(Figure 3.10) depicts the oscillatory WSSs corresponding the Power Law model from T_1 through T_6. During the entire cardiac cycle WSSs are found be to considerably large in all the outlet regions, owing to the reduction in their cross-sectional area. But for the early systolic time (T_1), considerably large and temporally oscillating, WSS bands are noted in the head and toe regions of AAA during the rest of the cardiac cycle. The hull of AAA is found to be subjected to periodically varying stresses which attain their maximum during the peak systole. Relatively large but oscillatory WSSs which attain their maximum around the peak systole are found across the entire cardiac cycle in the RIIAS region.

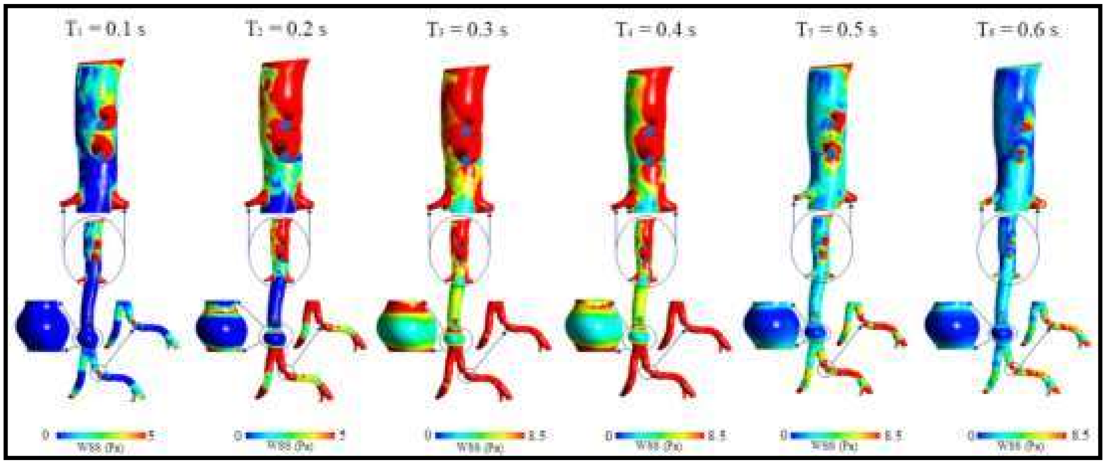

Figure 3.10 : WSS distribution along the aorta wall at the systole instants at T_1, T_2, T_3, T_4, T_5 and T_6 in the Power model

3.3.4.4 Herschel-Buckley model WSS

The WSSs corresponding to the Herschel-Buckley model as depicted in (Figure 3.11) are found to get large during the peak systole (T_3) through mid-systolic-deceleration (T_4). During the rest of the cardiac cycle, they are found to be relatively small across the entire arterial network barring the RIIAS region. It is also seen that relatively large WSSs are found during (T_2-T_6) especially in RIIAS region with the peak values during T_3 – T_4 cardiac instants. Also, large WSS bands especially in the head and toe regions of AAA are noted during the (T_3-T_6) cardiac instants, with relatively large and intense WSS bands during peak systole down to mid-systolic deceleration phase.

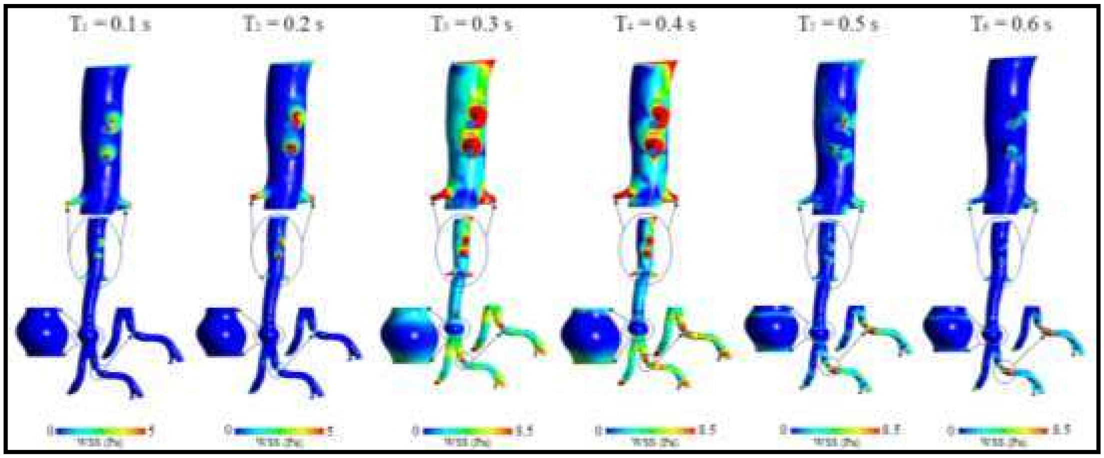

Figure 3.11 : WSS distribution along the aorta wall at the systole instants at T_1, T_2, T_3, T_4, T_5, and T_6 in the Herschel B model

3.3.4.5 Newtonian model WSS

Unlike the other models with the Newtonian model as seen from the plots under (Figure 3.12) one can notice that the WSS contours undergo multiple temporal WSS oscillations on the arterial wall during the accelerating and decelerating cardiac cycle phases (from T_1 to T_6). The WSSs which are relatively large during the early systole (T_1) go down during mid-systolic acceleration only to shoot up significantly in selective regions like the head and toe of the AAA, RIIAS region and iliac arterial regions. These stresses again go down during the late systolic time to early diastolic time in the entire network barring the RIIAS region including in its downstream vicinity. Here again large WSS bands are noticed during, T_1, (T_3-T_5) cardiac instants in head and the toe regions of AAA. Also, the WSSs in the toe region of AAA are found to be larger than those in the head region which go on to indicate that the toe regions are relatively more susceptible for damage.

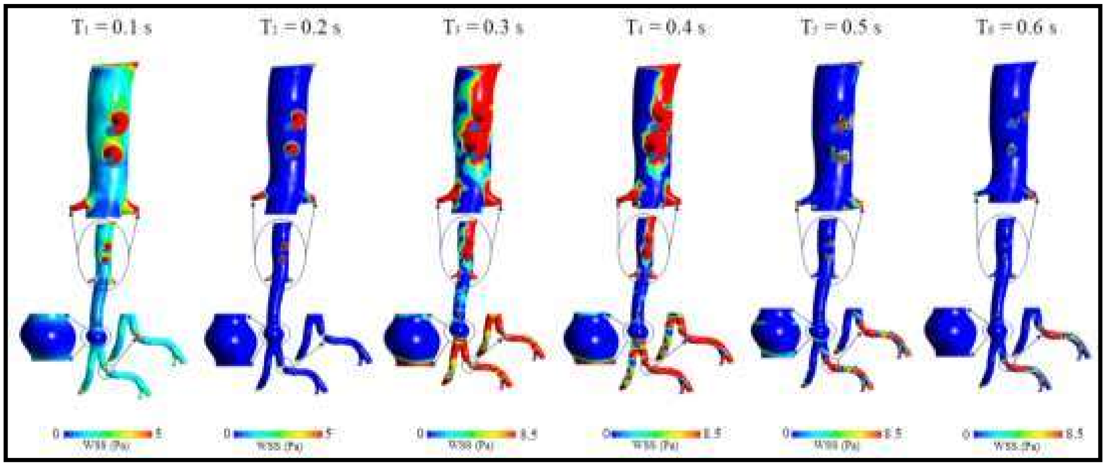

Figure 3.12 : WSS distribution along the aorta wall at the systole instants at T_1, T_2, T_3, T_4, T_5 and T_6 in the Newtonian model

3.3.5 Sensitivity of the WSSs

The above discussion clearly depicts the sensitivity of the WSSs to the rheological model and in the Tables (3.3 - 3.6) below the maximum WSSs at typical critical points in the AAA and RIIAS regions corresponding to different models are presented at different the cardiac instants at which these extreme values are noticed. The maximum WSS data at the typical critical points on AAA and RIIAS regions are not only in tune with the detailed investigation provided above but also clearly re-iterates its oscillatory nature and sensitivity to the rheological model for the blood. Especially in the clinical diagnostic context this data will be helpful in providing bounds on WSSs irrespective of the rheological model and thereby provides another useful heuristic in inferring the criticality level of the compounded pathological condition like the one considered in this study.

In effect, one can infer that the space-time average (STA) WSSs across the entire arterial network turns largest for the Cross model and relatively smallest for the

Herschel Buckley model during entire cardiac cycle. The STA WSSs corresponding to the Power Law model, Newtonian model and the Carreau Model follow in that order between the Cross and the Herschel Buckley models. While the WSSs corresponding to the Cross, Power Law and the Newtonian models are larger even during the early systolic phase and continue to grow till peak/mid systolic deceleration, the WSSs corresponding the Carreau and the Herschel Buckley model get significant during the peak systole and remain larger till mid-systolic deceleration. While WSSs corresponding to all the four non-Newtonian models depict a single space-time oscillatory behavior during the cardiac cycle the WSSs corresponding the Newtonian fluid depict multiple space-time oscillatory behavior in WSS. Also, the above results indicate that the cross model depicts a maximum variation in hemodynamics parameter results like WSS, WPs, centerline velocity and pressure. So, we now, address the issue of non-Newtonian importance factor (NNIF) as discussed in the literature (Johnston et al., 2004; Karimi et al., 2014a) for enabling a focused further exploratory study.

- **Coordinates of points P_1 (X = -0.0317718, Y= -0.0608621, Z= -0.306268) on RIIAS surface**

Table 3.3. Local WSS on selected point on the RIIAS surface

Cardiac instant (s)	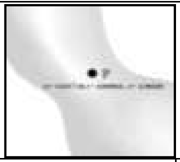	Local maximum WSS on selected point of the RIIAS wall surface			
	WSS_{max} (cross model) (Pa)	WSS_{max} (carreau model) (Pa)	WSS_{max} (HB model) (Pa)	WSS_{max} (power model) (Pa)	WSS_{max} (newtonian model) (Pa)
T_1	4.23	0.01	0.01	4.50	4.55

T_2	4.65	0.52	1.51	5.00	3.56
T_3	9.52	5.25	7.25	8.00	7.25
T_4	9.21	6.25	7.65	7.85	7.45
T_5	7.51	7.12	6.25	7.02	7.68
T_6	6.25	7.85	6.01	6.55	7.02

- **Coordinates of points P_1 (X= -0.0364554, Y= -0.0713144, Z= -0.253135) on AAA surface**

Table 3.4. Local WSS on selected point (P_1) on the AAA surface

Cardiac instant (s)	 Local maximum WSS on selected point of the AAA wall surface				
	WSS_{max} (cross model) (Pa)	WSS_{max} (carreau model) (Pa)	WSS_{max} (HB model) (Pa)	WSS_{max} (power model) (Pa)	WSS_{max} (newtonian model) (Pa)
T_1	3.12	0.01	0.12	0.12	1.12
T_2	3.88	0.01	0.12	3.45	0.01
T_3	4.12	5.65	3.24	7.54	1.54
T_4	7.12	5.35	2.35	6.54	1.35
T_5	3.6	1.52	1.52	4.56	0.85
T_6	3.5	0.51	0.85	2.65	0.12

- **Coordinates of points P_2 (X= -0.0321869, Y= -0.072469, Z= -0.263915) on AAA surface**

Table 3.5. Local WSS on selected point (P_2) on the AAA surface

Cardiac instant (s)	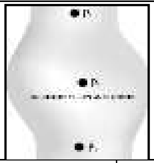	Local maximum WSS on selected point of the AAA wall surface			
	WSS_{max} (cross model) (Pa)	WSS_{max} (carreau model) (Pa)	WSS_{max} (HB model) (Pa)	WSS_{max} (power model) (Pa)	WSS_{max} (newtonian model) (Pa)
T_1	2.5	0.01	0.01	0.02	0.01
T_2	3.5	0.00	0.00	0.02	0.01
T_3	3.12	0.50	0.50	5.25	0.12
T_4	2.52	0.45	0.45	6.21	0.01
T_5	1.11	0.01	0.01	1.51	0.01
T_6	0.50	0.01	0.01	1.65	0.01

- **Coordinates of points P_3 (X= -0.0373254, Y= -0.0695855, Z= -0.274954) on AAA surface**

Table 3.6. Local WSS on selected point (P_3) on the AAA surface

Cardiac instant (s)	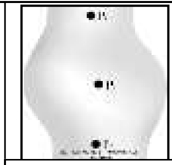	Local maximum WSS on selected point of the AAA wall surface			
	WSS_{max} (cross model) (Pa)	WSS_{max} (carreau model) (Pa)	WSS_{max} (HB model) (Pa)	WSS_{max} (power model) (Pa)	WSS_{max} (newtonian model) (Pa)

T_1	4.12	0.12	0.12	0.12	0.12
T_2	4.56	0.12	0.12	4.54	0.12
T_3	4.98	7.84	2.35	7.25	7.52
T_4	7.98	7.88	3.65	7.55	7.56
T_5	6.88	6.52	3.12	5.54	5.54
T_6	6.89	1.02	0.52	4.54	0.56

3.3.6 Non-Newtonian importance factor

To determine the impact of non-Newtonian models on WSS distributions, the global non-Newtonian significance factor, $\overline{I}_G$ is computed as follows:

$$\overline{I_G} = \frac{1}{N}\frac{\left[\sum_{i=1}^{N}(\mu-\mu_\infty)^2\right]^{1/2}}{\mu_\infty} \qquad (7)$$

Where i is the grid node index and incorporates the cells on the wall, N is the number of total grids, μ_∞= 0.00345 (kg/m s) represents Newtonian blood viscosity, and μ is the actual dynamic viscosity of blood. The $\overline{I_G}$ clearly tells us about the qualitative divergence of a blood rheological model from that of a Newtonian model for blood. Here the local deviation in dynamic viscosity of rheological models from that of a Newtonian fluid is averaged and is compared with dynamic viscosity of a Newtonian blood model.

Numerical values of $\overline{I}_G$ for four rheological models are provided in Table 7 at the six instances of the cardiac cycle. Clearly the $\overline{I}_G$ values corresponding to the Cross and Power Law models dominate in that order over the other two models during the entire cardiac cycle. From (Figure 3.13) one can be observe that among all four Non-

Newtonian viscosity models Cross and Power Law models show significantly higher values of $\bar{I}_G$ during T_3 , T_5 and T_6 as compared to other instants. During peak of systole Cross and Power Law models depict almost similar I_G values. Also, as the flow accelerates from the start to the peak of the systolic phase the $\bar{I}_G$ values increase and as the flow decelerates the I_G values decrease for both the Cross and Power Law models. Although at T_2 and T_4 these models are found to have similar pattern of velocities their $\bar{I}_G$ values vary at these cardiac instants. However, during the flow deceleration phase both their $\bar{I}_G$ values and the flow fields are found to vary significantly. This indicates that the blood rheology has greater influence during the flow deceleration phase wherein complex flow dynamics are noticed.

In the present work, the procedure used to find cut-off $\bar{I}_G$ values is similar to Safoora et al. (Karimi et al., 2014b), Johnston et al. (Johnston et al., 2004), and Soulis et al. (Soulis et al., 2008). While for a coronary artery in (Johnston et al., 2006) Johnson et al have taken the cut-off $\bar{I}_G$ value as 0.24 the same is taken as 0.15 by Safoora et al (Karimi et al., 2014b) for thoracic aorta. In this study, following the logic similar to that in (Johnston et al., 2006; Karimi et al., 2014b) since the Carreau Model and the Herschel Buckley Model depicts similar velocity, pressure and stress patterns like that of a Newtonian model the apt cut-off value is taken as $\bar{I}_G = 0.02$. For substantiating this cut-off value the $\bar{I}_G$ value is calculated for all the six-time steps of the cardiac cycle for all the Non-Newtonian models and these values are shown in Table 3.7. By looking at obtained results for $\bar{I}_G$ with plots of WSS distribution, it specifies that for time correspond to $\bar{I}_G < 0.02$ Carreau and Herschel Buckley models give WSS values closer to the Newtonian model from the start of systole to end-systole whereas the Cross and the Power Law model values differ significantly from those of the Newtonian Model. Both the Cross model and the Power Law model exhibit a trend line of increasing and decreasing $\bar{I}_G$ values with the pulsatile velocity. Further the Cross Model depicts the largest deviation from the Newtonian model at all instants of a cardiac cycle. In general, the numerically calculated $\bar{I}_G$ discloses that (a) rheological models of blood are essential in the low and peak velocity zones, (b) considering the cut of value $\bar{I}_G$ since the Cross and the Power Law model different significantly from that of the Newtonian model in the case of our study with an arterial network having multiple pathologies like AAA and RIIAS it can concluded that a Non-Newtonian model is more suitable in a multiply affected arterial network having AAA and RIIAS, (c) though the Power Law and the Cross Model are showing similar behavior the later model (Cross) may be preferred, as it depicts greater deviation from the Newtonian Model though both models depict similar the WSSs and WPs.

Table 3.7. Global importance factors for non-Newtonian models at six-time points over the cardiac

Cardiac time step size	Carreau model	Cross model	Power model	Herschel B model
T_1=0.1s	0.0121092	0.196921	0.033576	0.024381
$T_{2=}$ 0.2s	0.007534	0.208398	0.025661	0.017336
T_3=0.3s	0.002631	0.230581	0.223661	0.004116
T_4=0.4s	0.003517	0.229942	0.135661	0.005583
T_5=0.5s	0.006387	0.212721	0.017732	0.012836
T_6=0.6s	0.004763	0.203846	0.014532	0.007120

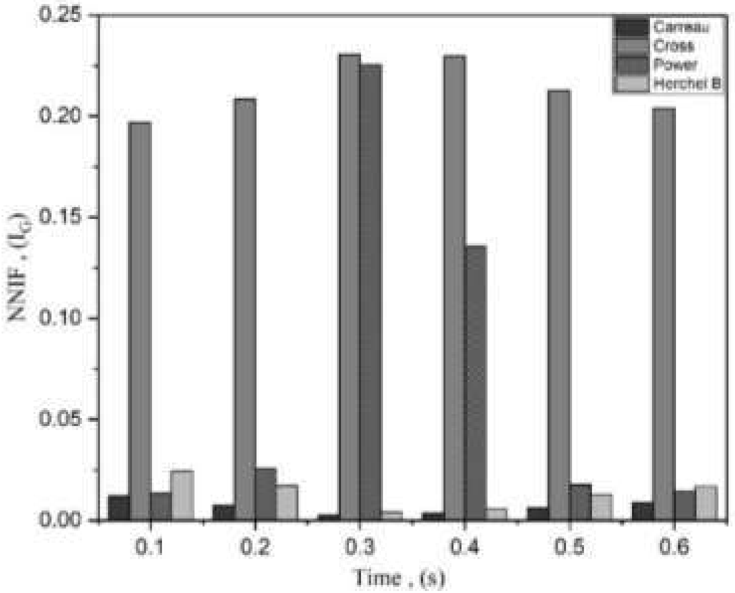

Figure 3.13 : Histogram of global non-Newtonian importance factor values at T_1, T_2, T_3, T_4, T_5 and T_6.

3.3.7 Non-Newtonian effect factor

The current study examines the effects of five blood viscosity models on the distribution of non-Newtonian effect factor (NNEF) and WSS under pulsatile blood flow situations. (Figure 3.14) depicts the non-Newtonian effect factor (NNEF), which is the relative difference between Newtonian and non-Newtonian WSSs. NNEF at a point P (X, Y, Z) on the surface of the arterial network wall was defined by Ardakani et al. (Jamalian Ardakani et al. 2010) as:

$$NNEF_P = \left(\frac{(WSS)_{non-Newtonian} - (WSS)_{Newtonian}}{(WSS)_{Newtonian}}\right)_P \times 100 \qquad (8)$$

Low wall shear stress is well known to promote intercellular permeability and consequently the vulnerability of certain vascular areas to atherosclerosis (Fox & Hugh 1966; Chiu & Chien 2011). As a result, a little change in low shear zones is more significant than one in high shear regions. This is why the relative difference (Eq. 8) is more useful than the absolute difference. (Figure 3.14) illustrate that the maximum deviation of the cross model from the Newtonian model arises on the outer curvature of the artery in which the lowest and highest values of WSS are observed. Between all five rheological models, the cross-model in (Figure 3.14) reveals the highest discrepancy from the Newtonian model. Also, from the (Figure 3.14) it is amply clear that while the WSSs on the outer surface of the arterial network under consideration is quite large, throughout the cardiac cycle, both for the Newtonian Model and Cross Model with the values for Cross Model being always dominant. Consequently, the NNEF for the Cross Model turns out to be both prominent and significant across the entire arterial network with space-time varying peaks zones. During the late diastole and the early systole (T_6-T_1) these peaks are noted in the branching zones, tapering iliac arterial zones and RIIAS region. During the systolic acceleration to the peak systolic phase (T_2-T_4) the large NNEFs are noted across the entire network with prominent zones in the RIIAS, iliac arteries and in all branching regions. During the late systole (T_5) the NNEFs are noticed majorly in the iliac arterial regions. In effect, during the entire cardiac cycle Cross Model NNEFs are quite large.

From all the above results corresponding to the five rheological models on hemodynamics and by comparing corresponding I_G values and NNEF values, it is to be noted that cross model has distinctly different characteristics from other rheological models. Hence, the further study is focused in unraveling the physics associated with the intricate flow dynamics of the Cross Model in terms of velocity variations, vortex formations, vortex shedding and flow swirling intensity.

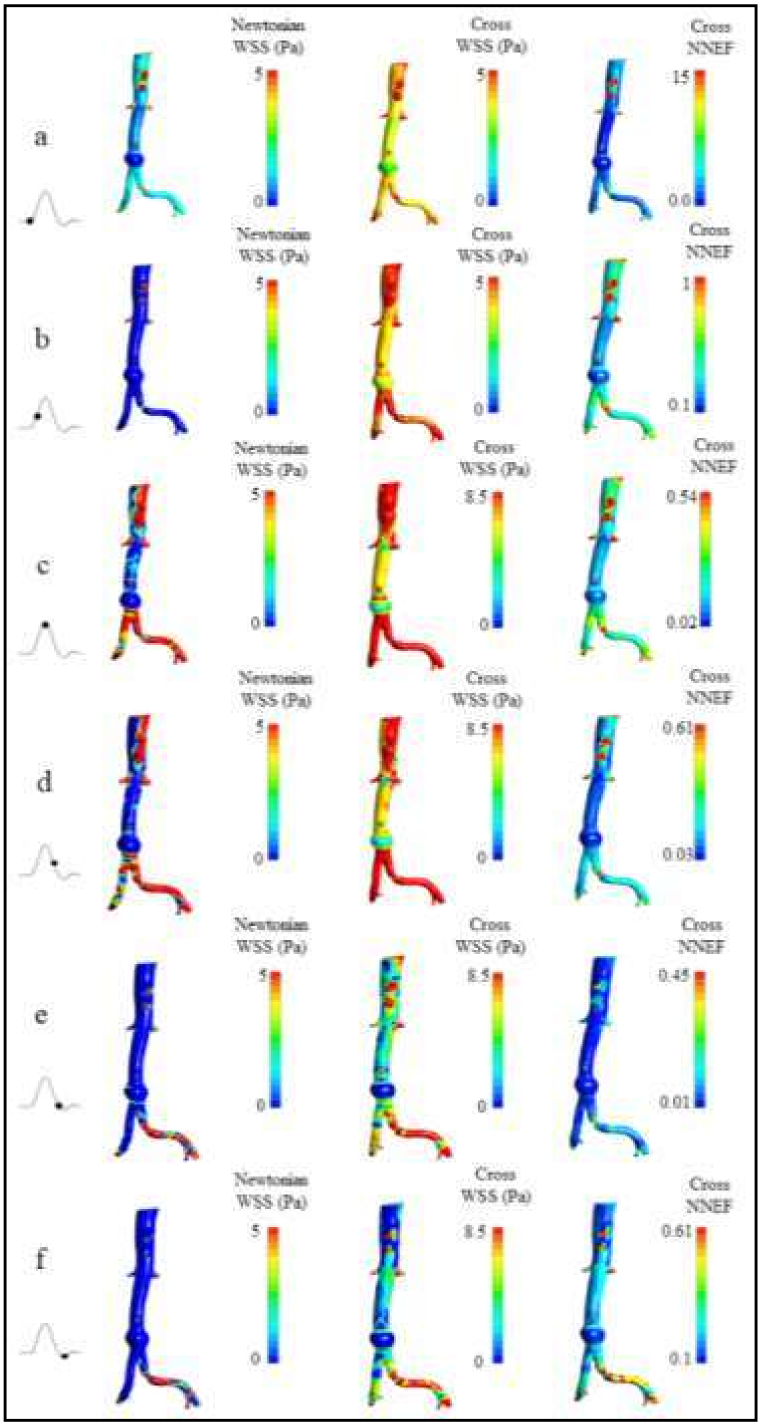

Figure 3.14 : WSS distribution along the descending abdominal artery wall during important time instant i.e. (T_1, T_2, T_3, T_4, T_5 AND T_6) and the non-Newtonian effect factor (NNEF) which is the relative difference between the Newtonian and non-Newtonian results is also shown.

3.3.8 Axial velocity contours

(Figure 3.15 (a) & (b)) depict the locally scaled axial velocity contours during systolic and diastolic phases in the Cross model. The results corresponding to axial sections S6, S7, S8 for (AAA); and S11, S12, S13 for (RIIAS) are presented here. In (Figure 3.15) (a) the velocity contours at different cardiac instants on the cross-sections S6, S7 and S8 which are at the entrance, middle, and at the end of AAA region respectively are presented. In (Figure 3.15 (b)) the velocity contours on the cross sections S11, S12 and S13 which are at the start, middle, and at the end of RIIAS region respectively are depicted at different instants of the cardiac cycle. As seen in (Figure 3.15 (a) as the flow rate through the artery is constant; because of the cross-sectional variation along the artery, the magnitude of blood flow velocity varies depending on the area of cross-section. During entire cardiac cycle the cross-sectional velocities on S7 are always lower than those corresponding to S6 and S8. On all the three sections the velocities are seen to increase with the systolic acceleration and decrease with the systolic deceleration but with an intensity and a space-time difference due to their cross-sectional variations. While on the section S6 and S8 the velocity magnitude variation is noted prominently on nearly the entire lumen of the cross section barring the wall region the same for the S7, corresponding the hull region of AAA, seem to be largely limited the core region of the cross section cantered on the central line of the vessel. Post axial section S7, the influence of dilation is noted on section S8, in which velocity is skewing toward to the posterior section of the wall during the cardiac cycle. When all five rheological models are compared, it is discovered that the cross model had a markedly dissimilar velocity waveform in all cross-sections than the other models.

Figure 3.15 (b) present the velocity contours on the cross-sections of RIIAS region, in which the velocities are always maximum on the S12 due to the sudden reduction in the diameter of the artery due to stenosis. The same on the sections S11 and S13, though lower but are comparable to those on S12. The velocities on S13 depict a relatively larger boundary effect than those on S11 especially in the late systolic and early diastolic phase. The skewness in the velocity magnitude contours especially on S13 indicates presence of complex flow dynamic features like flow separation, flow swirling, vortex formation etc. The three-dimensional detailed visualization of blood flow on the critical cross-sections, along the central axis of the entire arterial network, for the cross model is shown in (Figure 3.16) at the peak systolic instant (T_3) of the cardiac cycle. The velocity intensity variation patterns across the length of the arterial network clearly depict the presence flow complexities such as secondary flow, recirculation and vortex generation, which are further explained in the results to follow. Clearly, the velocity is higher across the stenosis region as compared to the region of the aneurysm in the arterial network.

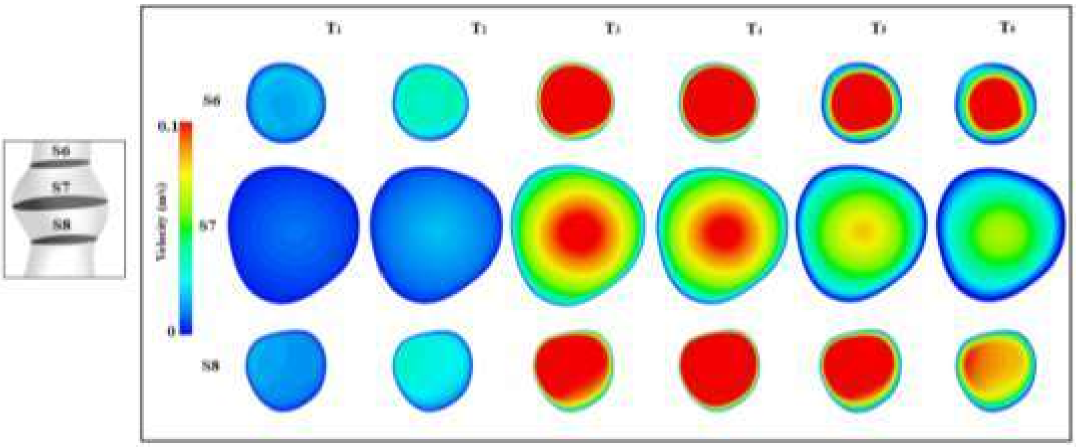

(a)

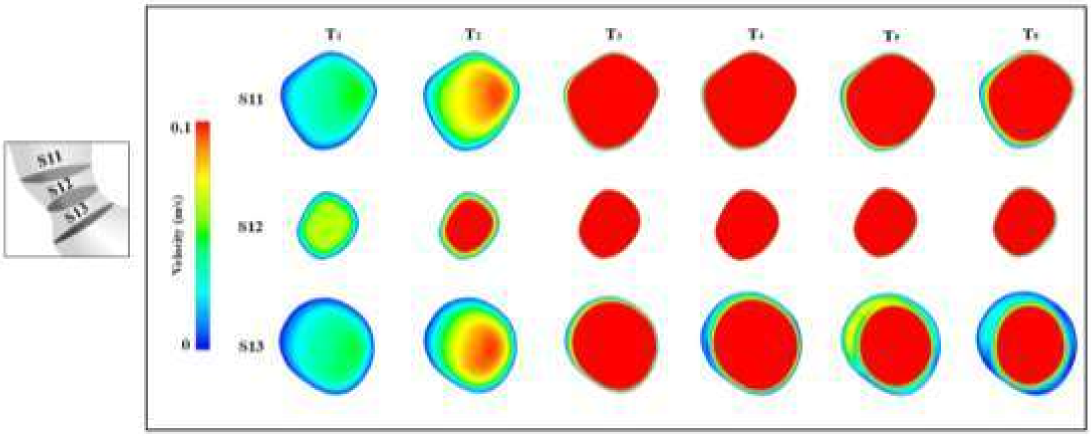

(b)

Figure 3.15 : (a) Velocity contours across the cross section S6, S7 and S8 of abdominal aortic aneurysms (AAA) at T_1, T_2 T_3 T_4 T_5 & T_6 in Cross (Crs) model (b) Velocity contours across the cross section S11, S12 and S13 of stenosis (RIIAS) at T_1, T_2 T_3 T_4 T_5 & T_6 in Cross (Crs) model.

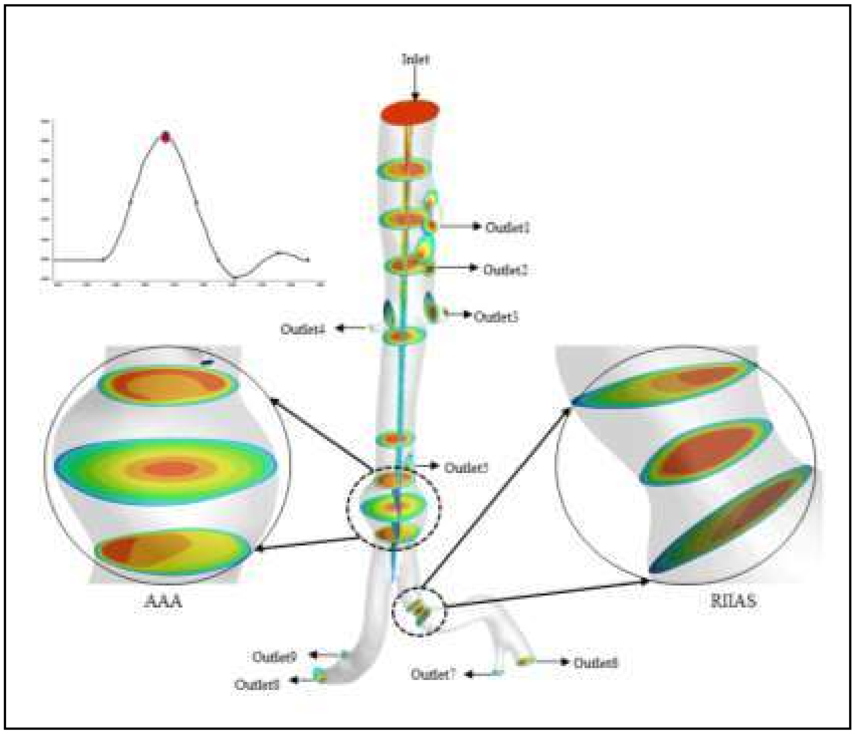

Figure 3.16 : Visualization of velocity contour at a different time step of the cardiac cycle also across various sections.

3.3.9 Streamlines of blood flow

Figure 3.17 (a) & (b) present the blood streams corresponding to the Cross model during the peak of systole, mid systolic deceleration phase, end systolic deceleration phase and at the start of diastole. The intricate pattern of streamlines, flow recirculation, vortices, and reverse flow behavior during the peak systole are vividly clear from the plots under the (Figure 3.4 & 3.5). During the T_3 and T_4 the streamlines corresponding to the flow are almost uniform throughout the model, excluding the RIIAS region especially during T_4. However, during T_5 many recirculation zones, vortex formation especially in the post stenotic region are noticed. During $T_{6,}$ i.e., at the start of diastole across the RIIAS region, skewness in flow, swirling inflow and prominent flow circulation zones as shown in the circled region in Fig 16. are noted. In addition, significant recirculation zones in the blood flow can be noted across the anterior and posterior regions of AAA. Blood flow becomes erratic around the inferior RIIAS, resulting in recirculation and reversed flow. There are flow separation zones downstream of RIIAS. The flow field shows clearly the complexities resulting from AAA, which are further exacerbated by RIIAS. It is quite clear that during the diastolic phase, the blood flow field is significantly affected by the geometrically variations in the arterial vessel which are brought in by the diseased conditions like AAA and RIIAS. Also, it may be noted flow field variations and velocity intensities and their respective variations across the RIIAS region are much larger than those across AAA region.

From above results a lot of randomness in the streamlines especially distal to the right iliac stenosis is noticed. This indicates the presence of highly oscillatory wall shear stress and turbulence mixing in the blood flow. Low and high oscillatory blood flow are linked with atherogenesis and plaque development (Slager et al., 2005). Hence for complex degree of stenosis turbulent model is imperative to be explored (Arun Mahalingam, Udhav Gawandalkar, Girish Kini, Abdulrajak Buradi, Tadashi Araki, Nobutaka Ikeda, Andrew Nicolaides, John R Laird, Luca Saba, 2016). The exactness of CFD models in forecasting hemodynamics parameters is significant and helpful in cardiac clinical decision support systems because plaque rupture is associated with critical flow and stress/strain circumstances at the stenotic cross section.

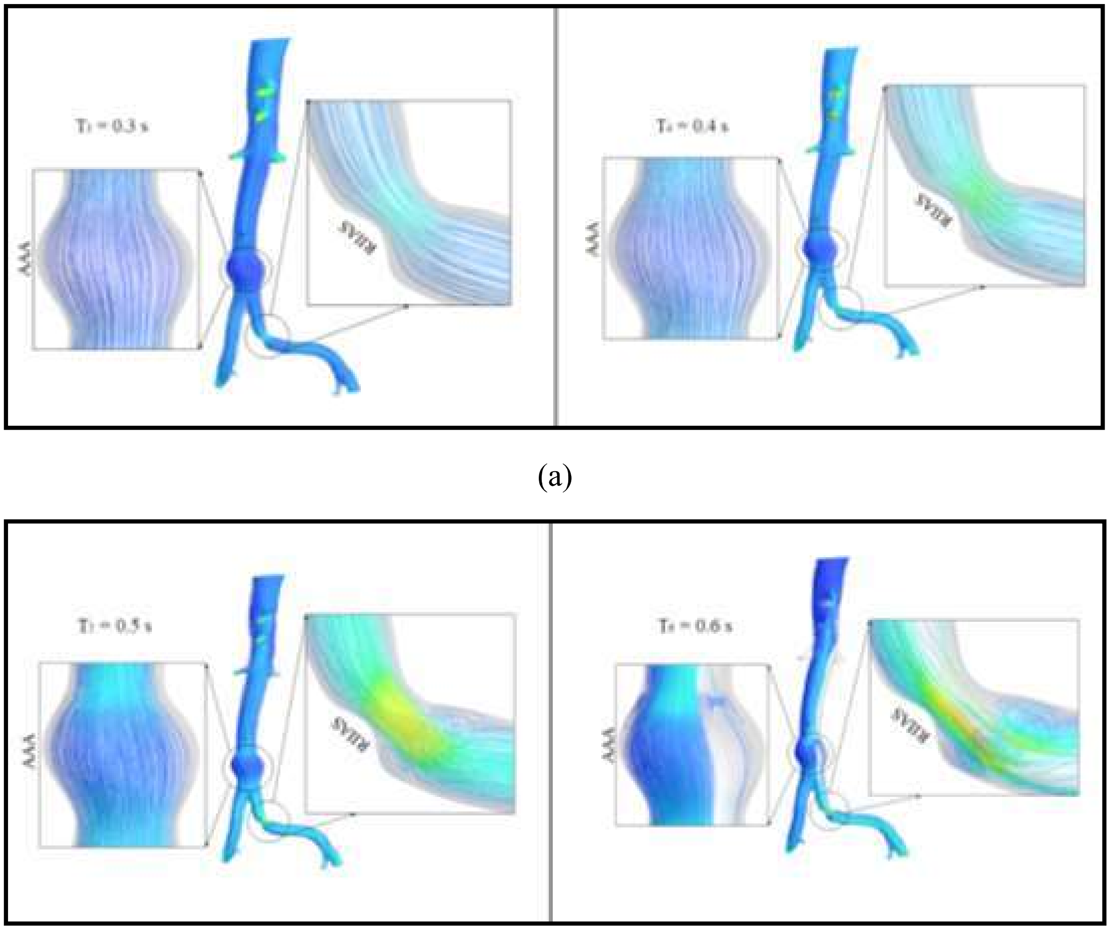

(a)

(b)

Figure 3.17 : Streamlines of blood flow in the cross model during (a) T_3 and T_4 (b) T_5 and T_6

3.3.10 Vorticity and Swirling Strength distribution

3.3.10.1 Vorticity

(Figure 3.18) demonstrates the 3D vortex core iso-surface in the cross model during significant six cardiac instants, i.e., T_1 to T_6 of the cardiac cycle. The swirling flow of blood in the flow field is referred to as a vortex. The quantity of vorticity is well understood to indicate energy concentration, flow situations, and the spatial condition of blood dynamics. From the iso-surface of vorticity, it has been observed that from the start of systole T_1 to the peak of systole T_3, the distal vorticity from RIIAS towards outlet 6 and 7 are reducing but from T_4 to T_6, its almost negligible, as shown in (Figure 3.18).

3.3.10.2 Swirling effect

In blood vessels, whirling flow improves oxygen transmission and lowers low-density lipoprotein absorption by improving cross-plane mixing. Since there are fewer studies on the swirling effect of flow dynamics, it is crucial to understand the flow dynamics behavior regarding swirling strength distribution. (Figure 3.19) depicts that the swirling strength from start of systole to end of systole in one cardiac cycle during which the development of some vortices near the wall region of aneurysms and pre and post stenosis, as shown by the black encircle in (Figure 3.19). The blood flow dynamic features observed in this study would be helpful for controlling the hemodynamic features through stents and vascular grafts, as they can partially restore the deformed arterial vessel to its original state to an extent.

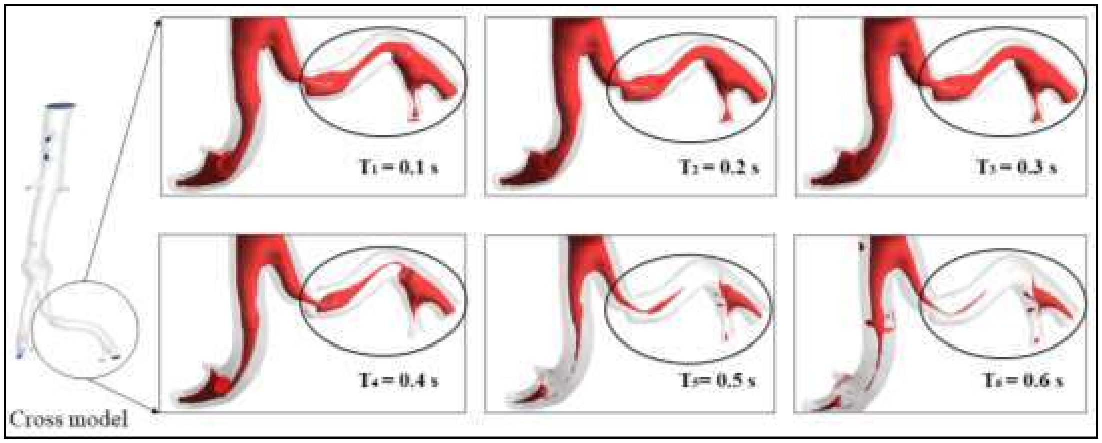

Figure 3.18 : Iso-surface of vorticity core region derived from of cross model during the systolic phase of the cardiac cycle

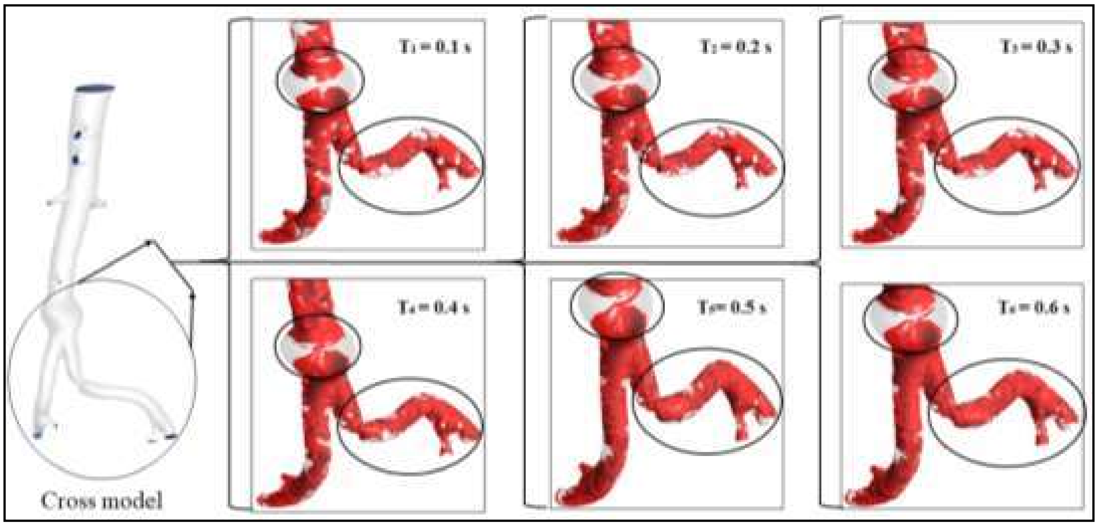

Figure 3.19 : Swirling strength distribution in one cardiac cycle T_1 to T_{6} = 0.1 to 0.6 s in cross model

3.4 Discussion

The efforts to assess hemodynamics non-invasively is critical not only for improving current disease monitoring practices, but also for developing patient-specific intervention to improve treatment efficacy and patients quality of life (Chen et al., 2006; Kenjereš, 2016). Blood flow dynamics in diseased arteries are influenced by dynamic viscosity. Despite decades of research using CFD to understand blood flow dynamics (Abbasian et al., 2020b; Antonova, 2012; I.E VIGNON-CLEMENTEL, 2018; Karvelas et al., 2022; Kenjereš, 2016; Kumar et al., 2022; Pandey et al., 2020a, 2020b; Philip et al., 2022) there is an inadequate understanding of how discrepancies in blood rheological models may affect the results obtained from these simulations. This is, to the best of the authors' knowledge, the first complete investigation to demonstrate the differences created by five important blood viscosity models using physiologically relevant arteriosclerosis models with pulsatile input flow. The Finite Volume Method (FVM) is used in this study for computational purposes. Because of its enormous versatility in discretization methods on structured and unstructured grids, the FVM in CFD is favored. Since the discretization is executed accurately in physical space and doesn't call for any transformation for computational purposes, this method is very adaptable (Le Dret and Lucquin, 2016). FVM can therefore be regarded as an appropriate method for taking fluid fluxes in complicated and irregular geometries into account. Additionally, continuity, momentum, and energy equations are discretized in a clear manner in the FVM numerical method. This approach favors the integral form of conservative legislation over their differential form (Blazek, 2015). In terms of significant gradients over a control volume, the approach thus provides more precision and stability. In this work we continued our studies on same previous geometry (Kumar et al., 2022) consisting AAA and RIIAS but here the four physiologically significant rheological models has been considered for understanding the discrepancy between models during cardiac cycle.

3.5 Principal Findings

Previously, most of the researchers have studied ascending abdominal arteries. The authors suggest the downward abdominal arterial network in this paper, compounded by multiple diseased conditions like AAA and RIIAS and outlets, including bifurcations with realistically tapering lumens and investigate the flow dynamics corresponding to five rheological models. This study is further extension of our previous work (Kumar et al., 2022) in which geometry is generated by considering the D/L_a of AAA and D/L_s of RIIAS an vital role in deciding the diseased region and its failure predictions. In this work, while the AAA is at moderate level (i.e., at 47 % of fusiform blowup) the RIIAS is at the severity of 91% constriction. However, altering the amount of dilatation and shrinkage in the same artery may influence the mechanical properties of the wall. RIIAS can cause a decrease in arterial blood in the iliac artery. This decreased blood supply to the human body's lower extremities might induce tingling of the organs in that region.

Several theoretical, computational and experimental studies related to the pulsatile blood dynamics in the vicinity of stenosis, aneurysms, bifurcations, and bends have been carried out. However, the exact nature of fluids, i.e., rheological models, mechanical effects, and connection with the physiological response, is not fully understood. From Figure (3.4 - 3.5) our results depict that both the centerline velocity and wall pressure in a doubly afflicted diseased model vary for all five rheological models with the cardiac cycle. However, the results corresponding to the cross model are closer to those of the Newtonian model.

In Figure 3.6. (a) and (b) it is shown that the WSS magnitudes corresponding to the Cross and Power models are greater than the other three rheological models all along the curve AB at the peak, the middle of deceleration, and the end of systole. Variations in regional WSS occur because the arterial vessel wall enlarges just prior to bifurcation and then contracts just after. The complexity of the flow, including separation, vortex formation, vessel curvature, flow whirling, etc., may also have a role in the occurrence of severe oscillatory WSSs in the post-stenotic area. From Figure 3.7 (a) and (b) it is observed from the wall pressure (WP) distribution of five rheological models that the increase in the WPs especially in the AAA region, due to the wall dilation, very well agrees with the fall in the central line velocities in the same region noted earlier. The complex WP patterns indicates the presence of complex flow variation in the downstream of RIIAS.

Tables (3.3- 3.6) show how sensitive the WSSs are to the rheological model at typical critical points in the AAA and RIIAS regions. These critical WSS corresponding to dissimilar models are seen at different times in the cardiac cycle. In the clinical diagnostic context this data will help to set limits on WSSs, no matter what rheological model is used. This gives a qualitative and quantitative way to figure out the quantum of influence of a combined pathological condition like the one considered in this study on the blood flow dynamics of a patient. This simulation helps the people working in the field of physiological fluid dynamics as well as the medical practitioners. Current practice in the clinical context for diagnosing diseased arteries is to measure some basic features like localized blood flow rate and blood pressure. It is important to find how pressure and wall shear stress vary along the entire arterial network. In silico approach can provide such a detailed qualitative and quantitative information (Boutsianis et al., 2009b; Kung et al., 2011). Understanding blood rheology is critical for this, which can be accomplished by using continuum constitutive models for stress-strain variation during the cardiac cycle. By this surgeon can have access to artery structure as well as complete knowledge of blood flow behavior in multiple healthy and diseased conditions. In turn it will enable them to draw conclusions from their diagnostic tools such as Angiography, Magnetic Resonance Imaging (MRI), and Magnetic Resonance Angiography (MRA) etc., for coming up with an effective, robust and precise remedial measures for treating the diseased subjects. Also, it is found from the results of the numerical simulations that the size and shape of aneurysm and stenosed vessels does influence the blood flow. A little change on the cross-sectional value makes vast change on the blood flow rate. Also, blood flow under multiple diseased condition of an artery has extremely complex phenomenon. The design of vascular prostheses, i.e., the creation of artificial organs, also necessitates prior understanding of the blood flow distribution in both healthy and sick arteries. The construction of the extracorporeal system necessitates a comprehensive understanding of the fluid dynamics and morphology of the system in question. The pre-identification of hotspots will aid physicians in deciding how to improve the focused medicine distribution.

3.6 Limitations and extensions

Rigid boundary conditions have been assumed for that arterial wall, and blood vessel motion during the cardiac cycle was not considered in this study. Also, more studies need to be performed on outlet boundary conditions like using the open loop conditions etc. with better material properties of blood while calculating the kinematic co-efficient of viscosity for different rheological models and more accurate using CT/MRI Image data and better reconstruction of the patient-specific geometry through iso-geometric analysis. Here blood is not treated as thixotropic or elastic as the study is dealing with large blood vessels.

3.7 Summary

In this study, detailed alterations in flow dynamics due to the presence of multiple complexities due to aneurysms and stenosis are traced. It is focused on identifying clinically useful bounds on physiological flow indicators such as WSS, WPs etc., encompassing the flow dynamics of different blood rheological models as per the geometrical variations due to the pathological complexities. The variations in flow complexities captured through WSS, velocity contour, swirling strength, vorticity, and streamlines depict that the blood flow dynamics as traced by Cross and Power Models considerably differ from those of other models. This study leads to the following conclusion:

- During peak of the systole, there is significant diversity in velocity curve response in all five models, although the cross model is closer to the Newtonian model in the context of trend line and behavior. The pressure magnitude is larger in the AAA zone and an adverse space-time alternating pressure gradient is seen in the RIIAS region due to its stenosed state.
- The localized rheology-based variations, particularly in the RIIAS region, such as spatial lag in oscillatory peak WSS manifestation and downstream post-stenotic region oscillatory WSSs, can be attributed to flow complexities such as separation,

vortex formation, swirling along the vessel curvature. Also, the periodically varying complex WP patterns noticed in the RIIAS region and in its downstream region can lead to instability in blood flow due to vortex generation and vortex shedding leading to complex downstream flow dynamics.

- While WSSs corresponding to all the four non-Newtonian models depict a single space-time oscillatory behavior during the cardiac cycle, the WSSs corresponding the Newtonian fluid depict multiple space-time oscillatory behavior in WSS. Also, the Cross Model depicts a maximum variation in hemodynamics parameter results like WSS, WPs, centerline velocity and pressure.
- The NNEF contours corresponding to the five blood viscosity models depict that the Cross Model has particularly different rheological characteristics from other rheological models.
- The modelling findings show that at low inlet velocity i.e. (start of systolic and diastolic phase), the distribution of WSS for cross and power model are considerably different from other rheological models. The significant differences in WSS values are mainly detected around the superior part of the artery wall along the inlet to outlet 4, AAA and RIIAS region, and the inferior region of lower outlets. Also, the velocity distribution especially in the AAA region and RIIAS region significantly vary with prominent changes especially during the early diastole in the posterior region to RIIAS with recirculation zones, reversed flow patches, intensified flow swirling etc.

- From results of non-Newtonian importance factor (I_G) for various rheological models it is proposed that $\bar{I}_G \sim 0.02$ is an appropriate non-Newtonian blood activity cut-off value in the descending abdominal artery having AAA and RIIAS.
- The study discovered high wall shear stress spectrums and wall pressure bands on aneurysm and stenosis head/toe regions during late systole. Maximum WSSs in critical locations such as AAA and RIIAS can aid in clinical diagnosis.

When researching into the simulation results, keep in mind that the blood vessel wall is believed to be rigid. This assumption is critical in the accumulation of energy through the systolic and diastolic periods of the heart cycle. For improved approximations, moving wall boundary conditions must be defined in numerical computations to include blood vessel deformability.